Structural and Thermal Characterization of Oxy-Halide Materials for Solid State Batteries

Master's Thesis

Master of Materials Science

Nxumalo Siyabonga Blessing

Supervisor:

Dr. Zsolt Kovasc

Eötvös Loránd University (ELTE)

Faculty of Science

Department of Materials Physics

Budapest, 2020

STATEMENT OF INTELLECTUAL PROPERTY

Name: Nxumalo Siyabonga Blessing

Neptun ID: IDYQFH

ELTE Faculty of Science:MSc Materials Science

specialization:

Title of diploma work: Structural and Thermal Characterization of Oxy-Halide Materials for Solid State Batteries

As the author of the diploma work, I declare, with disciplinary responsibility that my thesis is my own intellectual product and the result of my own work. Furthermore, I declare that I have consistently applied the standard rules of references and citations.

I acknowledge that the following cases are considered plagiarism:
– using a literal quotation without quotation mark and adding citation;
– referencing content without citing the source;
– representing another person's published thoughts as my own thoughts.

Furthermore, I declare that the printed and electronical versions of the submitted diploma work are textually and contextually identical.

Budapest, 20

_____

Signature of Student

Abstract

Batteries are a key component in tools humans use in everyday life. Intensive research is constantly being done to improve their power capacity, energy density, increasing shelf life and safety. In this research, a new class of lithium-rich anti-perovskite materials have been subjected to structural and thermal characterization for solid state batteries as substitutes for currently used organic liquid electrolytes which are toxic and flammable. Past research has shown that this new class of lithium-rich anti-perovskite materials have a low energy barrier for ionic transport and are able to accommodate many mobile Li ions in the crystal lattice. Three lithium-rich anti-perovskite samples (Li_3OCl, Li_3OCl-Ba and Li_3OCl-Ca) were prepared and analysed using X-ray diffraction, thermal differential analysis, the rate at which they decompose when exposed to moisture and used to assembled coin cells. X-ray diffraction was used to identify the different crystalline/semi-amorphous phases in the sample. Differential thermal analysis was used to determine different calorimetric data and phase transitions during heating and cooling cycles. The samples were then used to assembled coin cells for ionic conductivity measurements. After immediate assembly, the cells were connected to a circuit with 1.4A current. A potential different of 2V was recorded across the cell, showing that materials do enable Li ion transport. It is important to mention that the prepared are highly hygroscopic and were mostly kept in an Argon filled glove box to protect them from moisture; the samples readily decompose when exposed to moisture. In conclusion of the research, the extent of hygroscopicity of the samples was examined by exposing them to moisture and observing their relative weight change as they absorb moisture.

Acknowledgements

In conclusion of this research, I would like to firstly acknowledge my supervisor, Dr Zsolt Kovacs, who played a key role to its completion. He did not only provide technical input towards my research, but he also continuously motivated me to finish this thesis. I would also like acknowledge Dr Fabian Margit, Istvan Tolni, Mr Oka and other people who played who helped me conduct and analyse all my experiments. This research would not been completed without their input. Lastly, I would like to thank my friends and parents for being my pillar of support in every time of need.

Contents

Chapter 1: Introduction 7

1.1. Problem Statement and Significance 7

1.2. Research Objectives 9

Chapter 2: Literature Review 10

2.1. How Batteries Work 12

2.2. The Development of Lithium-ion Batteries 15

2.3. Lithium-ion Batteries: Components and Assembly 17

2.4. Published Articles on Lithium-Rich Anti-Perovskite Materials as Electrolytes for Lithium-ion Batteries 19

2.4.1. Superionic Conductivity in Lithium-Rich Anti-Perovskites 21

2.4.2. Lithium and Chlorine-Rich Preparation of Mechanochemically Activated Anti-Perovskite Composites for Solid-State Batteries 22

2.4.3. Li-Rich Anti-Perovskites Li_3OCl Films with Enhanced Ionic Conductivity 22

Chapter 3: Methodology 24

3.1. Sample Preparation 24

3.1.1 Instrumentation 24

3.1.2. Experimental Procedures 26

3.2. X-ray Diffraction 27

3.2.1. Instrumentation 28

3.2.2. Experimental Procedures 29

3.3. Decomposition of Samples 30

3.3.1. Instrumentation 31

3.3.2. Experimental Procedures 31

3.4. Differential Thermal Analysis 32

3.4.1. Instrumentation 32

3.4.2. Experimental Procedures 34

3.5. Coin Cells 34

3.4.1. Instrumentation 35

3.4.2. Experimental Procedures 37

Chapter 4: Results and Discussion 40

4.1. Sample Preparation 40

4.3. Decomposition Rate 42

4.2. X-ray Diffraction 44

4.4. Differential thermal analysis 51

4.5. Cell preparation 59

4.5.1. Preparation of electrodes 59
3.5.2. Prepared of electrolytes 60
3.5.3. Coin cell assembly..... 61
Chapter 5: Conclusion and Recommendation 64
Chapter 6: Reference..... 66

Chapter 1: Introduction

As the world aims to decrease its dependence on fossil fuels and with advancements being made in information technology every day, batteries have become an essential mean of producing and storing electrical energy. They are a key component in tools humans use in everyday life. Batteries are found in almost all motor vehicles, all types of portable electronics, cordless tools, flashlights, smoke alarms, hearing aids, heart pacemakers, wrist watches, biomedical instruments, and in buildings to supply backup power (Yoshino, 2014).

Among the different types of batteries in the market, lithium-ion batteries find a wide range of applications in technologically essential fields. This is because of their long power capacity, high energy density, charge-discharge rate, and long cycling lifetime (Lu, et al., 2014). Even when compared to counterpart rechargeable batteries, lithium-ion batteries have better gravimetric and volumetric densities (Manthiram, 2017). The use of water-free, nonaqueous electrolytes enable lithium-ion batteries to operate at higher voltages of approximately 4V (Liu, Liu, Pei, & Cui, 2018). As a result, they are a power source of choice in portable electronic devices. Lithium-ion batteries are also being developed towards energy sustainability as an integration between wind, solar and carbon fuels. They are used in conjunction with solar panels to supply off-grid electricity in developing regions and are increasingly being used in developed regions together with gasoline to power electric vehicles (Zubi, Dufo-Lopez, Carvalho, & Pasaoglu, 2018). From portable electronics to a more environmentally friendly electricity mix with less fossil fuels, lithium-ion batteries have great prospects presently and for the future.

1.1. Problem Statement and Significance

Research and modifications are constantly being done on lithium-ion batteries to improve their power capacity, energy density, service life, and more importantly, to improve

their safety. Accidents involving fires and explosions frequently occur when they are discharged and/or charged improperly. Fires and explosions occur when the exothermic reaction in the battery goes out of control, leading to thermal runaway. Incidents involving cell phones, laptops, electric vehicles, and airplanes have been recorded worldwide. Some incidents have threatened human life and others have led to product recalls by manufacturers. Incidents that have received media attention include the Tesla electric car battery fire, the Boeing 787 Dreamliner, and the Samsung Galaxy Note 7 (Liu, Liu, Pei, & Cui, 2018). There are many efforts being employed to improve the safety of lithium-ion batteries. These efforts include external and internal protection mechanisms. Temperature sensors and pressure valves are being installed in electronic devices as an external protection measure. Unfortunately, these mechanisms increase the dead weight/volume of the battery and are sometimes unreliable in harsh thermal or pressure conditions. Internal protection mechanisms are said to be far more reliable and sustainable. These include using reliable materials to construct battery components: selecting safer anode and cathode materials and using safer electrolytes (Liu, Liu, Pei, & Cui, 2018).

This research aims at investigating the structural and thermal characterization of oxy-halide materials, as a safer substitution for currently used electrolytes, for solid state batteries (lithium-ion batteries to be specific). The electrolyte in most lithium-ion batteries is a nonaqueous electrolyte solution containing $LiPF_6$ or $LiBF_4$ dissolved in a carbonate compound mixture. Generally, the electrolyte is a mixture of organic solvents and an electrolyte salt compound (Yoshino, 2014). The mixture of organic solvents usually contains cyclic carbonate esters, linear carbonate esters and diethyl carbonate. For the electrolyte solution to allow free transport of Li ions, it must have a high dielectric constant and low viscosity. Cyclic carbonate esters have a high dielectric constant but high viscosity, and the opposite applies for linear carbonate esters; hence they are mixed (Yoshino, 2014). Even though the electrolytes transport

Li ions efficiently, they are toxic, corrosive, and volatile (Fabian , et al., 2021). Not only do they contribute to the fires and explosions associated with lithium-ion batteries, but they also pose a threat to the environment when poorly discarded because of their corrosive nature.

1.2. Research Objectives

A new class of lithium-rich anti-perovskite, Li_3OX (X= Cl, Br, etc.), materials are currently being investigated as potential electrolytes for high-performance solid-state batteries. This new class of materials are solid and readily decompose to environmentally friendly components when exposed to moisture, removing the current dangers posed by the liquid electrolyte being used. Research has shown that this new class of materials have a low energy barrier for ionic transport and are able to accommodate many mobile Li ions in the crystal lattice. Lithium-rich anti-perovskite materials can attain ionic conductivities of 10^{-3} Scm^{-1} when doped with a cation or anion (Lu, et al., 2014).

In this research, three lithium-rich anti-perovskite materials are being proposed as solid electrolytes for high-performance solid-state batteries. The samples are Li_3OCl, Li_3OCl-Ba (Li_3OCl doped with a little Ba), and Li_3OCl-Ca (Li_3OCl doped with a little Ca). The samples were prepared and analysed using X-ray diffraction, differential temperature analysis, change in weight when exposed to the atmosphere, and used to assemble coin cells. A detailed explanation of how the samples were prepared, analysed and the results obtained can be found in subsequent chapters.

Chapter 2: Literature Review

A battery is defined as an assembly of electrochemical cells attached together electrically in series and/or in parallel to generate a desired voltage and current. A battery supplies a direct current that always flows in one direction, unlike the alternating current supplied to our homes through the electrical grid (Cairns, 2004). The electrochemical cells that makeup batteries consist of a negative electrode (the anode), a positive electrode (the cathode), an electrolyte contained in between the electrodes, and a container or housing (Yoshino, 2014). A general schematic of a Zn-Cu electrochemical cell, called the Daniell cell, can be seen in figure 1 below. The schematic contains labels of the different components (anode, cathode, and electrolyte) that make up the cell and the redox reactions occurring in the cell.

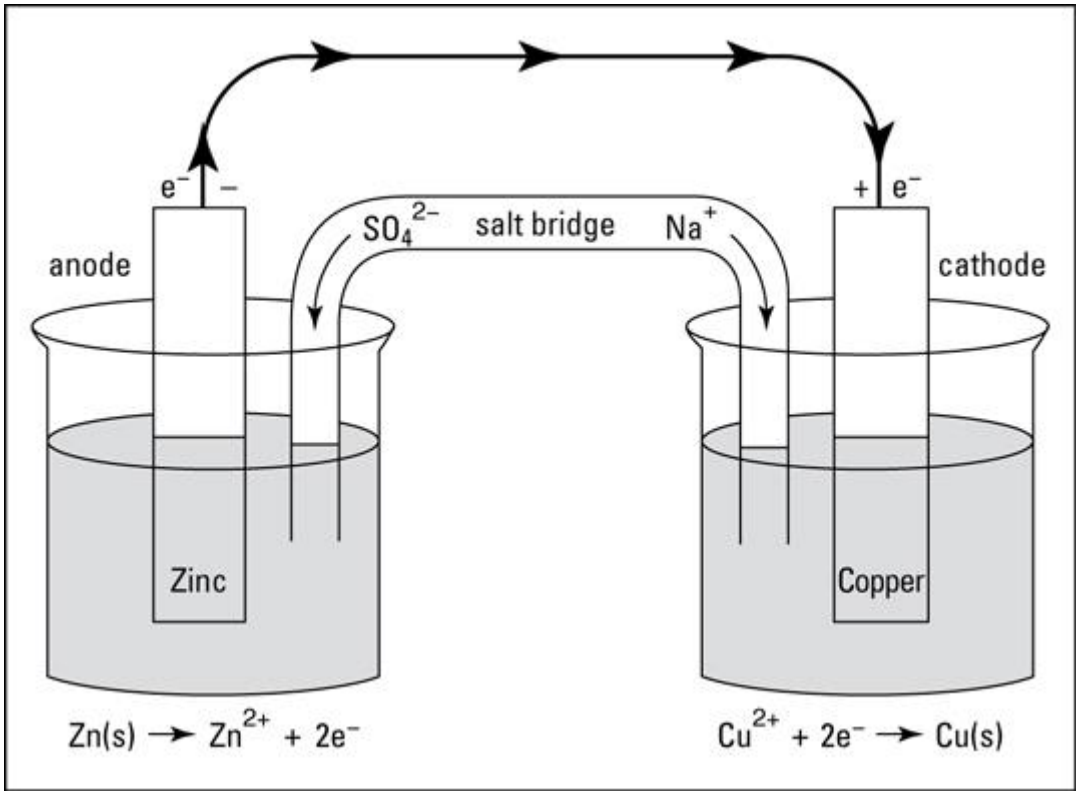

Figure 1: A Daniell electrochemical cell (John Wiley & Sons, Inc., 2011)

Batteries are broadly classified as primary or secondary batteries. Primary batteries can only be discharged once and are then discarded; they cannot be recharged. Rechargeable

batteries are called secondary batteries (Shah Bukhari, Maqsood, Baig, Ashraf, & Khan, 2015). They are recharged by forcing the current though the electrochemical cell in the opposite direction, reversing the electrochemical reaction that occurred during discharge. Primary and secondary batteries are further classified according to the electrode material and type of electrolyte (polymer, ceramic, molten salt, organic, and aqueous) used (Cairns, 2004). In Table 1, a few examples of different batteries have been categorized by their ability to be recharged or not, according to the electrode material and electrolyte used in the cell. Some of their applications have also been mentioned in the table.

Battery name	Primary (non-rechargeable) or secondary (rechargeable)	Electrode Material	Electrolyte	Applications
Zinc-carbon battery	Primary	Zinc and manganese dioxide	Aqueous (potassium hydroxide)	Flashlights
Zinc-air battery (Zn-air)	Primary	Zinc and porous catalysed carbon	Aqueous (potassium hydroxide)	Hearing aids, film cameras
Lithium ion manganese oxide battery (Li-MnO2)	Primary	Lithium and manganese dioxide	Organic solvent (Li salt in ethylene carbonate)	Utility meters, tracking devices
Lithium ion Disulphide (Li-FeS_2)	Primary	Lithium and iron disulphide	Molten salt (mixture of alkali metal chlorides)	Military applications where burst of power is required
Lead-acid battery (Pb-PbO_2)	Secondary (1st rechargeable Battery)	Lead and lead dioxide	Aqueous (sulphuric acid)	Starting automotive engines
Edison cell (Ni-Fe)	Secondary	Nickel and oxyhydroxide	Aqueous (potassium hydroxide	Railway vehicles
Lithium-ion battery	Secondary	Metal oxide ($LiCoO_2$) and carbonaceous material (graphite)	Organic solvent (Li salt in ethylene carbonate)	Portable electronics

Table 1: examples of different batteries and their classifications (Cairns, 2004)

2.1. How Batteries Work

Batteries produce electrical energy as a result of spontaneous electrochemical reactions in their cells. These reactions are driven by the Gibbs free energy and can be calculated from

data obtained in tables of thermodynamic properties (Cairns, 2004). The maximum voltage an electrochemical cell can generate can be calculated using the equation below:

$$E = -\,{}^{\Delta G}/_{nF} \qquad (1)$$

where *E* is the voltage produced by the cell (units: volts), ΔG is the change in Gibbs free energy of electrochemical reaction in the cell (units: joules/mole), the number of electrons taking part are represented by *n* (units: mole), and F is Faraday's constant (96487 coulombs/mole). From the above equation, one can deduce that a large negative value for the Gibbs free energy favours the electrochemical reaction in the cell and yields a high cell voltage.

Another important property of batteries is their specific energy. A battery's specific energy is the amount of energy it can store per unit mass, expressed in watt-hours of energy per kilogram (Wh/kg = 3.6 kJ/kg). By further assuming excess electrolytes and negligible mass at the terminals, the theoretical specific energy of a battery can be deduced (Cairns, 2004). The theoretical specific energy (u) is the maximum specific energy that is attained from a certain mass of reactant materials in the battery, expressed in the equation below:

$$Theoretical\ specific\ energy = -\,{}^{\Delta G}/_{\sum Mw} \qquad (2)$$

The theoretical specific energy is at its maximum when Δ*G* has a large negative value and $\sum Mw$, the summation of equivalent weights of the reactants taking part in the electrochemical reaction, is small. Large values of Δ*G* are attained by choosing highly electropositive materials to construct the negative electrode. These materials readily give off electrons. On the other hand, electronegative materials, materials that easily accept electrons, should be used for the positive electrode. Furthermore, one should select materials that yield a small summation of equivalent weights as the reactants in the electrochemical cells, making the term $\sum Mw$ small (Cairns, 2004). Taking equations (1) and (2) into consideration is essential when selecting

which electrode materials to use in batteries. Generally, materials containing elements from the top left of the periodic table are used to construct the negative electrode. These elements are both electropositive and have smaller molecular weights. Elements from the top right of the periodic table are selected to construct the positive electrode; they are highly electronegative and have smaller molecular weights (Cairns, 2004). The figure below illustrates the cell voltage and theoretical specific energy for different batteries. The points on the plot represent theoretical maximum values calculated from thermodynamic data.

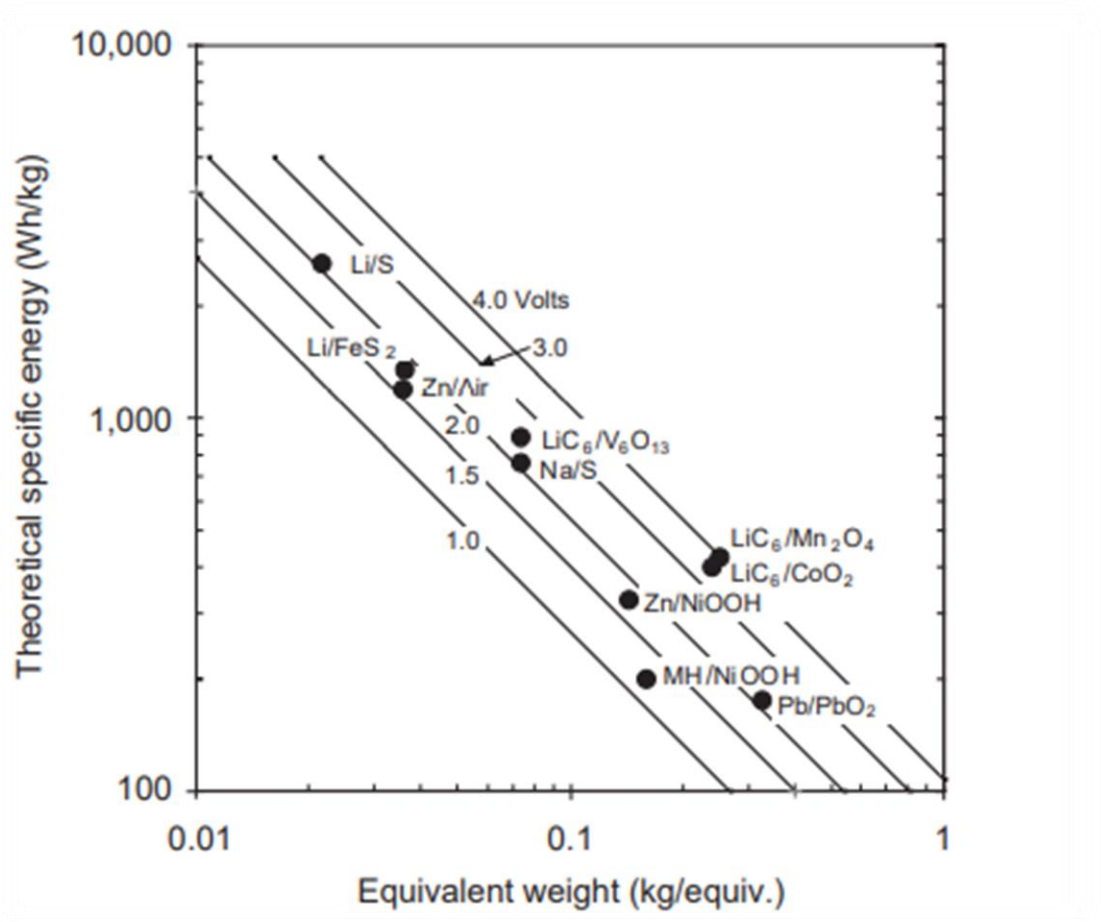

Figure 2: cell voltages and theoretical specific energies for different batteries (Cairns, 2004)

Practically, the specific energy for commercial cells falls within the range of one-fifth to one-third of the theoretical values. Even though the electrochemical reactions in the cells differ, they all follow the same principle (Cairns, 2004). Electrical energy is generated from the redox

reaction taking place between the two electrodes of the cell. Therefore, it is expected that cells having high equivalent weight materials like lead and lead dioxide have low specific energies.

2.2. The Development of Lithium-ion Batteries

The foundation of the field of battery science and engineering was laid by Volta's invention of the Volta pile in the early 1800s. The pile was assembled using silver, alternating layers of zinc, and an electrolyte drenched into leather or cardboard. Volta's invention inspired many more scientists to construct their own electrochemical cells to generate and store electrical energy. Even though the scientists had limited understanding of how the cells operated, they were able achieve significantly large currents at high voltages for relatively long periods (Cairns, 2004). We now know that Volta's cell generated electrical power by oxidizing zinc and reducing the native oxide layer on silver. By dismantling the cell and exposing it to air, the silver electrodes were oxidized, and the cell recharged (Cairns, 2004).

The generation of more electrochemical cells and batteries led to the development of the two-fluid cell by John F. Daniell in 1836. He used amalgamated zinc to construct the negative electrode and copper to make the positive electrode. The cell was assembled in large container with the copper electrodes placed in porcelain jars while surrounded by cylindrical zinc electrodes inside the container. As the name (two-fluid cell) suggests, two different electrolytes were used in the electrochemical cell: a solution of copper sulphate in the copper electrode's partition, and sulfuric acid in the zinc electrode partition (Cairns, 2004).

Sir William R. Grove, renowned for inventing the fuel cell, also assembled a two-electrolyte cell in 1839. Instead of copper, Grove used platinum placed in fuming nitric acid for the positive electrode, and zinc placed in sulphuric acid for the negative electrode (Cairns, 2004). Despite Volta, Daniell and Grove's success, their electrochemical cells were all primary cells and had to reassembled with new materials after discharge.

The first rechargeable battery was constructed by Gaston Plante in 1860. The battery's cells were erected using lead sheet electrodes and sulphuric acid as the electrolyte. The sheets were spirally twisted into a cylindrical shape with a porous separator placed in between them. Plante's cells achieved voltages of 2.0 V and the battery was charged using primary batteries (Cairns, 2004). Scientists such as Waldemar Jungner and Thomas Edison improved Plante's battery by experimenting with different electrode materials and electrolytes. They experimented with alkaline electrolytes and, many metals and metal oxides. These materials included zinc, cadmium, iron, copper oxide, silver oxide, and manganese oxide (Cairns, 2004). Jungner and Thomas' choice in electrolytes and electrode materials were aimed at minimizing the net consumption of the electrolyte in the cell reactions, which was a disadvantage of Plante's cell. By the beginning of the 20th century, a wide range of cells had been investigated and commercialized for different applications. Lead-acid, nickel-cadmium, and nickel-metal hydride batteries with aqueous electrolytes were the conventional rechargeable batteries available or under development at that time. However, these batteries had limitations on reducing the size and weight and increasing the energy density (Yoshino, 2014).

The 1980s came with advancements in information technology on portable electronics. These included the development of mobile phones, video cameras, and notebook computers (Yoshino, 2014). As a result, the demand for rechargeable batteries with greater capacity and reduced size and weight increased. This led to the birth of the battery at the centre of this thesis: the lithium-ion battery. With the limitations posed by the batteries being used, research in the early 1980s showed that lithium-ion batteries could be the solution (Yoshino, 2014). The first prototype of a lithium-ion battery was assembled in 1985 by Akira Yoshino. Yoshino based his assembly on previous research conducted by John Goodenough, M. Stanley Whittingham, Rachid Yazami and Koichi Mizushima. In 1991, Sony and the Asahi Kasei team led by Yishio Nishi commercialized the first lithium-ion battery (Li, Lu, Chen, & Amine, 2018). Following

their success, the market demand for lithium-ion batteries drastically raised, as shown in the figure below:

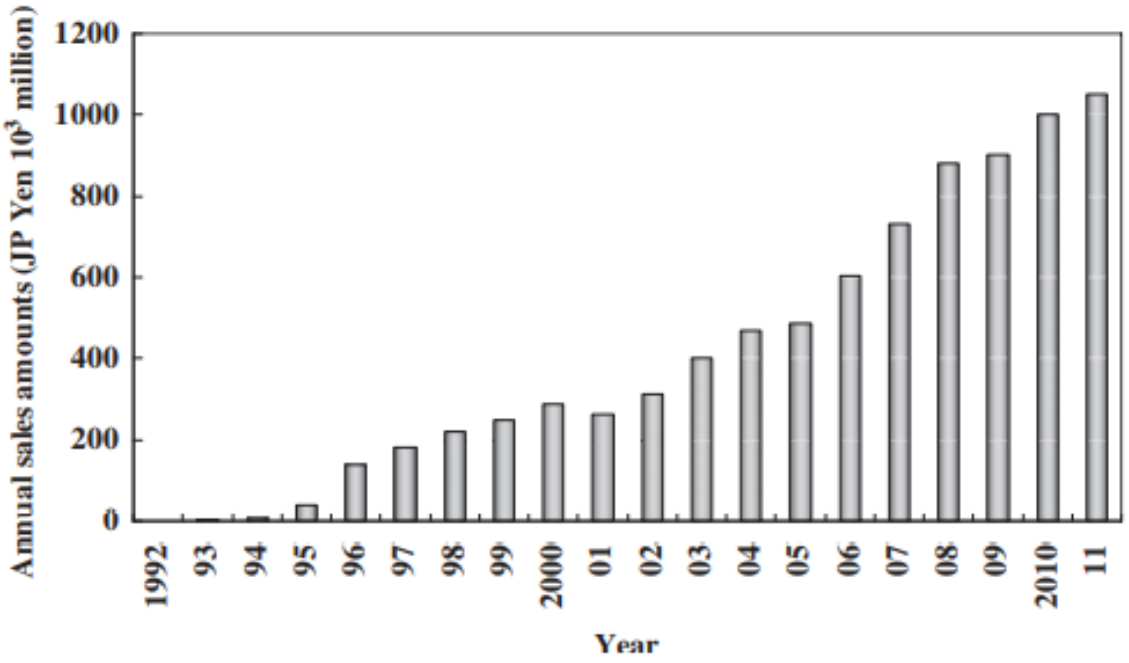

Figure 3: annual sales for lithium-ion batteries for the first 15 years on the market (Yoshino, 2014).

With more advancements being made in portable electronics, electric vehicles, and on lithium-ion batteries themselves, their market has further increased; they remain a dominant electrical energy storage solution.

2.3. Lithium-ion Batteries: Components and Assembly

Like most batteries, lithium-ion batteries are composed of four major components: the cathode, anode, electrolyte, and separator. Lithium cobalt oxide ($LiCoO_2$) and some form of carbonaceous material, like graphite, with a crystal structure are the most used materials for the cathode and anode, respectively. The combination of the two electrode materials enables cell reactions with little side reactions and no chemical transformation of electrodes. As a result, a stable battery with long service life, and good storage capacity is obtained. $LiCoO_2$

and the carbonaceous material are also stable materials in air; no special atmosphere is required for the battery (Yoshino, 2014).

Typical lithium-ion batteries are assembled by winding sheets of the cathode and anode material, with a separator membrane in between, inside a battery can. A multilayer electrode assembly is obtained with the electrode material coated on both sides of a current collector. Electricity is conducted by the current collector from the active electrode material to tabs connected to the electrode terminals. Aluminium foil and copper foil with 10μm thickness is used for the cathode and anode current collector, respectively. The battery can is then infused with a nonaqueous electrolyte solution containing $LiPF_6$ or $LiBF_4$ dissolved in a carbonate compound mixture and sealed (Yoshino, 2014). An example of a typical lithium-ion battery can be seen in the schematic below:

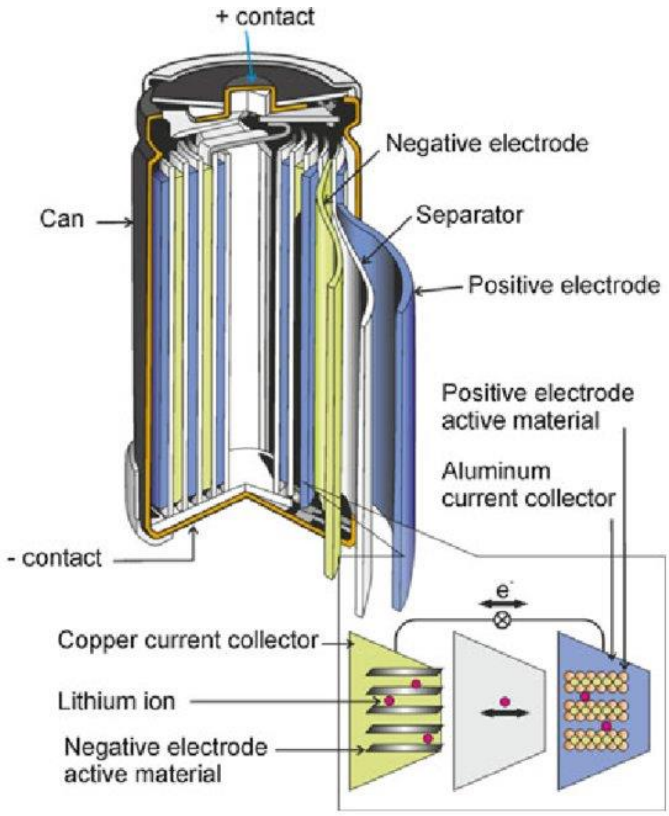

Figure 4: labelled schematic of a lithium-ion battery (Wagner, Preschitschek, Passerini, Leker, & Winter, 2013)

Lithium-ion batteries operate on the phenomenon of reversible intercalation of Li ions between the cathode and the anode, producing an average cell voltage of approximately 3.7V When discharged, Li atoms are only contained as part of the cathode. The atoms migrate from the cathode, through the electrolyte, to the carbonaceous material that makes up the anode during charging. Electrical energy in the battery is stored or released by repeating these processes reversibly (Yoshino, 2014). From when they were first commercialized by Sony in 1991, the energy density of lithium-ion batteries has drastically increased. Sophisticated lithium-ion cells can now achieve specific energy densities of approximately 250 Wh/kg (900kJ/kg). This amount can be further increased to 650 Wh/kg and 950 Wh/kg by using Li-S and Li-air systems, respectively (Liu, Liu, Pei, & Cui, 2018).

2.4. Published Articles on Lithium-Rich Anti-Perovskite Materials as Electrolytes for Lithium-ion Batteries

As mentioned above, the electrolyte in lithium-ion batteries is generally a mixture of organic solvents and an electrolyte salt compound. Research on the electrolyte solution is primarily centred around functional electrolyte additives, flame-resistant or non-flammable electrolyte solutions, and new electrolyte salts. Functional additives are added to the electrolyte solution to improve battery performance (Yoshino, 2014). Like in this research, finding flame-resistant or non-flammable electrolytes improves battery safety. Recent research on the same class of lithium-rich anti-perovskite materials has shown that they have the highest Li concentration of all Li-based solid electrolytes (Zhao & Daemen , 2012). They also display superionic conductivity, low activation energy, exceptionally low electronic conductivity, and offer a large voltage and current operation window. In addition, the low-cost starting materials to synthesize them suggests economic advantages (Yang, DeVita, Lee, & Kim, 2020).

Lithium-rich anti-perovskites are ionic compounds where the typical perovskite structure has been electrochemically inverted and Li^+ are located at the octahedral vertices of the structure. The typical perovskite structure has the form $A^+B^{2+}X^-_3$, where A is a monovalent metallic cation (e.g., Na^+), B is a divalent cation (e.g., Mg^{2+}), and X is a highly electronegative monovalent anion (e.g., F^-). In lithium-rich anti-perovskites, the highly electronegative anion has been replaced with the electropositive lithium metal; the divalent cation is now a divalent anion, oxygen; and the monovalent metallic cation has been replaced with the monovalent anion chlorine. As a result, a lithium-rich anti-perovskite compound with the form $ClOCl_3$ ($A^-B^{2-}X^+_3$) is obtained. By following the cation first inorganic nomenclature of ionic compounds convention, the ionic compound is rearranged to have the form Li_3OCl ($X^+_3B^{2-}A^-$). As mentioned above, Li^+ are located at the octahedral vertices of the anti-perovskite structure. Oxygen is located at the octahedral centre and chlorine is positioned at the dodecahedral centre of the structure. Figure 5 shows a schematic of the anti-perovskite structure. In figure 5, the purple balls represent the position Li^+, the grey balls represent Cl^- and the blue ball represents the position of O^{2-}.

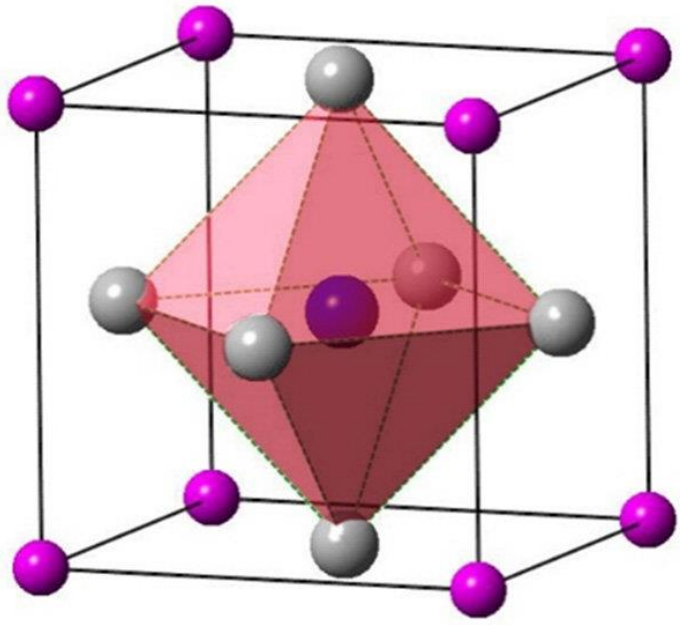

Figure 5: the anti-perovskite structure (Chen, Li, Hu, Chen, & Li, 2017)

Publications proposing the same class of lithium-rich anti-perovskite materials as a substitute for the currently used liquid electrolyte solutions are briefly explained below. It is important to note that the obtained results from these publications slightly differ but are consistent. Their slight differences are because of the different experimental procedures followed during sample preparation and measurement processes.

2.4.1. Superionic Conductivity in Lithium-Rich Anti-Perovskites

Three different lithium-rich anti-perovskite samples were prepared and analysed using X-ray diffraction, Differential Scanning Calorimetry, and Impendence Spectroscopy. The samples are Li_3OCl, Li_3OBr and $Li_3OCl_{0.5}Br_{0.5}$. The samples were prepared by first grinding the starting materials together using a mortar and pestle. The resulting paste was placed in quartz tube and heated to 330-360 under vacuum conditions for several days. During heating, water was effectively removed and condensed using a condensation trap and a high-vacuum pump. The resulting molten product was quenched or slow cooled, resulting in different textures and grain boundary morphologies. The general reaction equation of the samples can be seen below:

$$2\ LiOH + (1-z)\ LiA + z\ LiA' \longrightarrow Li_3OA_{1-z}A'_z + H_2O$$

Where A and A' are chlorine and bromine, respectively. The resulting lithium-rich anti-perovskites exhibited ionic conductivities greater than 10^{-3} S/cm at room temperature an activation energy of 0.2-0.6 eV. It was also observed that the ionic conductivity increases to advanced superionic conductivities greater than 10^{-2} S/cm as the temperature is increased towards the melting point (Zhao & Daemen , 2012).

2.4.2. Lithium and Chlorine-Rich Preparation of Mechanochemically Activated Anti-Perovskite Composites for Solid-State Batteries

Lithium oxychloride, Li_3OCl, was prepared and analysed using X-ray diffraction, scanning electron microscopy, and electrochemical impedance spectroscopy. The focus of this publication was to investigate the stoichiometry affects on phase stability and Li conductivity of the lithium-rich anti-perovskite, Li_3OCl. Molar ratios of 2:x of LiOH: LiCl were used to prepare the different samples where x was varied from 0.5, 1, 1.5, 2 and 2.5. The sample was prepared by heating the starting materials at 350ºC for 6 hours before being quenched to room temperature at ambient conditions. After quenching, the samples were transferred to an argon-filled glovebox to avoid exposure to air. The samples were then grinding using zirconia with high-energy ball-milling for 30 minutes and then analysed. The general reaction equation of the experiment can be seen below:

$$2LiOH + LiCl \longrightarrow Li_3OCl + H_2O$$

It was observed that Li_3OCl prepared with at least 100% excess LiCl exhibits cathodic stability against Li metal, showing stable interface properties. Furthermore, the solid electrolyte exhibited an ionic conductivity of $3.2*10^{-5}$ S/cm (Yang, DeVita, Lee, & Kim, 2020).

2.4.3. Li-Rich Anti-Perovskites Li_3OCl Films with Enhanced Ionic Conductivity

In this publication, thin Li_3OCl films were fabricated via pulse laser deposition. To fabricate the films, it was necessary to deposit desired anode, cathode, and electrolyte material into film format to form multi-layered films with good structural integrity and a controllable interface. The films were analysed using X-ray diffraction, impendence spectroscopy and used to assemble coin cells. The anti-perovskite solid electrolyte films showed enhanced ionic conductivity at room temperature by more than an order of magnitude in comparison to bulk produced Li_3OCl. This is attributed to the Li^+ and /or Cl^- vacancies and the preferential

orientation of the films. At room temperature, the ionic conductivity of the Li_3OCl films was measured to be $8.9*10^{-6}$ S/cm and $3.5*10^{-4}$ S/cm at 140°C. The temperature dependence of the films was then fitted with the Arrhenius equation to determine the activation energy as 0.36eV (Lu X. , et al., 2014).

Even though the obtained results are dependent on sample preparation and measurement processes, past research asserts that lithium-rich anti-perovskites offer great potential for high-performance solid-state batteries. The dependence of sample preparation and measurement process also offers room for more research when it comes to structural manipulation and electronic tailoring.

Chapter 3: Methodology

3.1. Sample Preparation

As mentioned in previous chapters, this research aims at investigating the structural and thermal characterization of oxy-halide materials, as a safer substitution for currently used electrolytes, for solid state batteries. The samples subject to investigation are listed below:

- Li_3OCl
- Li_3OCl-Ba: Li_3OCl doped with a little Ba
- Li_3OCl-Ca: Li_3OCl doped with a little Ca

The samples were prepared based on a study conducted by Braga et al. The general equation of their composition is $A_{3-2x}M_xO_{1+y}Cl_{1-2y}$ (where A=Li; M= Ba, and Ca; x= 0.005; y=0). The resulting samples are Li_3OCl, $Li_{2.99}Ca_{0.005}OCl$, $Li_{2.99}Ba_{0.005}OCl$, and $Li_{2.99}Mg_{0.005}OCl$. For simplicity, the samples are referred to as Li_3OCl, Li_3OCl-Ba and Li_3OCl-Ca in this research.

3.1.1 Instrumentation

3.1.1.1 High Precision Weighing Balance

A X Precision weighing balance was used to measure the stoichiometric weight of raw materials. High precision balances are ideal for small sample measurements as they give highly accurate results, within the milligram range. The X Precision weighing balance extends the accuracy to four decimal places.

Figure 6: X Precision weighing balance

3.1.1.2. Teflon Crucibles

The weighed raw materials were placed in Teflon PTFE crucibles for the reactions to take place. Teflon PTFE crucibles are excellent for heat transfer and can be used within temperature ranges of -200 to 250^{o}C. They are also non-wettable, unbreakable, lightweight, non-contaminating, and inert to chemical attack. This makes them highly favourable for producing the desired samples.

Figure 7: Teflon PTFE crucibles

3.1.1.3. Oven/furnace

A Memmert oven was used as an electrical furnace to melt the raw materials. Memmert heating and drying ovens are sold by Memmert USA. Memmert ovens are equipped with an AtmoControl software that enables the control of complex processes via Ethernet. They also have special accessories that allow the user to adjust or add features such as entry pots, interior lighting for observing loads, stacking frames, extended overtemperature protection, telescopic trays, heating and cooling temperature ranges, and gas concentration variations (oxygen, carbon dioxide and nitrogen).

Figure 8: Memmert Oven

3.1.2. Experimental Procedures

The samples were prepared by first weighing stoichiometric amounts of raw materials. Analytical grade commercial powders were used as raw materials. The Materials are LiCl, LiOH, Ca $(OH)_2$, and Ba $(OH)_2$ and were they purchased from VWR International

Company. After weighing, the raw materials were mixed and homogenized, and then placed in sealed Teflon crucibles. The crucibles were placed in the oven and heated 3 hours, while maintaining the temperature at 230^{o}C. This resulted in a solidified white bulk samples which was grinded by ball-milling using agate balls to particles sizes below 50μm. The resulting samples were placed and handled in a glove boxes filled with inert Argon (Ar) to protect them from moisture; the samples are highly hygroscopic and readily decompose to their starting materials when exposed to air. Reaction equations of how the samples were prepared can be seen below:

$LiCl + 2LiOH = Li_3OCl + H_2O$

$LiCl + 2LiOH + Ca(OH)_2 = Li_3OCl\text{-}Ca + H_2O + H_2 + O_2$

$LiCl + 2LiOH + Ba(OH)_2 = Li_3OCl\text{-}Ba + H_2O + H_2 + O_2$

3.2. X-ray Diffraction

Due to the uniform spacing of atoms in a crystal, incident beams of X-rays interfere constructively to form patterns that give information on the atomic and molecular structure of crystals. This phenomenon is called X-ray diffraction. Similar to the way a uniformly ruled grating act on a beam of light, atomic planes of crystals act on X-rays. This interaction is governed by Bragg's law. Bragg's law relates the spacing of atomic planes in crystals, the angle at which the planes constructively interference with incident beams of X-rays and the wavelength electromagnetic radiation. Bragg's law is illustrated in the schematic below:

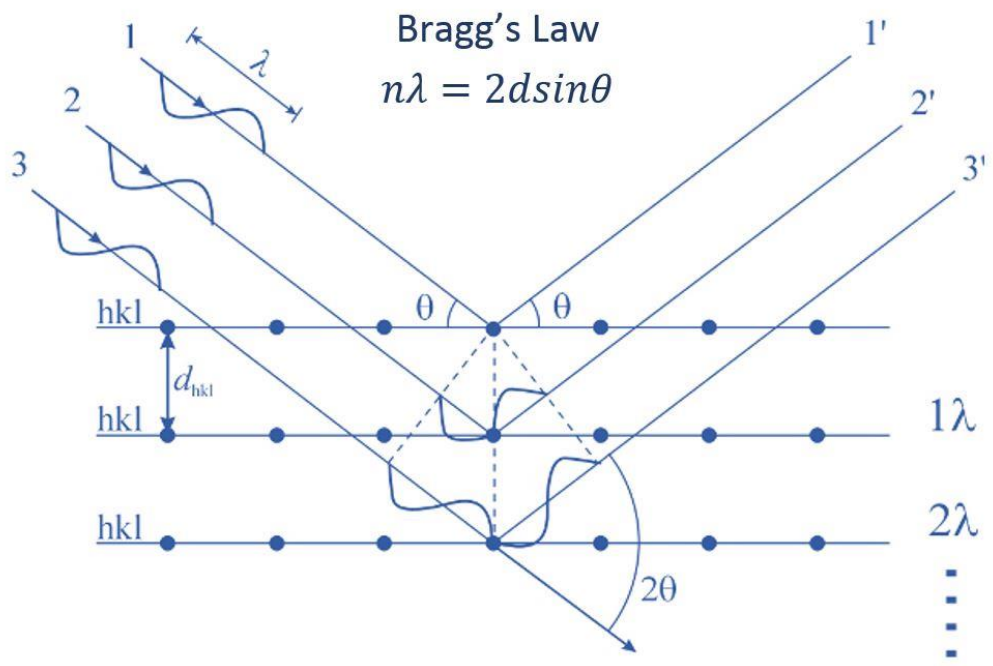

Figure 9: Bragg's law for most intense reflections of electromagnetic radiation (University of Illinois, 2014)

The diffracted X-rays are detected, processed, and counted. Three-dimension information on the atomic and molecular structure can be reconstructed by changing the geometry of the incident rays, orientation of the sample and the detector, and measuring the angles and intensities of these diffracted beams. In details, the average position of the atoms in the sample, their chemical bonds, crystallographic disorder, and various other characteristics of the crystalline materials can be measured.

3.2.1. Instrumentation

3.2.1.1 X-ray Diffractometer

A Rigaku Smart Lab X-ray diffractometer was used to conduct X-ray measurements of the samples. The diffractometer operates at 1.2kW and the measurements were conducted in the Bragg-Bentano mode. The diffractometer is also equipped with a

position sensitive silicon detector which measures in the so-called one-dimension mode instead of the usual zero-dimension mode.

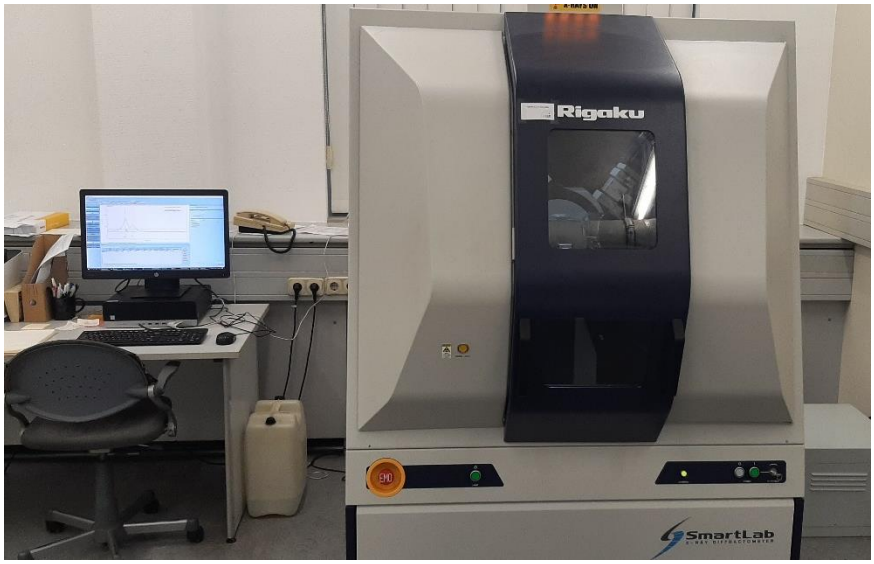

Figure 10: Rigaku Smart Lab X-ray diffractometer

3.2.2. Experimental Procedures

Because the samples are highly hygroscopic and readily decompose to their starting materials when exposed to air, they were placed on a glass plate and covered with plastic foil of 10μm thickness before diffraction measurements were conducted. The foil was selected among other covering materials by a series of X-ray tests to have minimum contribution to the X-ray spectra and allow ample time for X-ray diffraction tests in the air filled chamber of the X-ray diffractometer. All handling and preparation of the samples was conducted in a glove box filled with Argon. The prepared samples can be seen in the figure below:

Figure 11: Samples covered with plastic foil for X-ray diffraction

$CuK\alpha_1$ and $CuK\alpha_2$ X-rays with wavelengths of 1.54056 and 1.54439 Å were used to radiate the samples, respectively. Incident rays with an average wavelength of 1.54784 Å were produced. The measurements were conducted between 20^o and 100^o 2Θ angles at a speed of 0.025^o/s. Phases in the obtained spectra were analysed and identified using data from the ICDD database.

3.3. Decomposition of Samples

Hygroscopic substances tend to absorb moisture/water from the air. This generally occurs in room temperature to such an extent they will absorb a significant percentage of their weight in water. Hygroscopic materials are mostly salts; however, other materials do display this affinity to water property. The absorption of water molecules into the molecules of hygroscopic substance often results in physical changes. These changes involve an increase in volume, changes in colour, boiling point, temperature, and viscosity. As mentioned in previous chapters, the prepared samples are highly hygroscopic and readily decompose to their starting materials when exposed to air. The rate at which the samples decompose was determined by measuring the change in weight when exposed to air at room

temperature. Water is evaporated off the samples during preparation. During decomposition, this reaction is reversed, and water is therefore absorbed. The absorbance of the water is accompanied by a change in weight of the samples.

3.3.1. Instrumentation

3.3.1.1. High Precision Weighing Balance

A Sartorius weighing balance was used to measure the change in weight of the samples when exposed to air. High precision balances are ideal for small sample measurements as they give highly accurate results, within the milligram range. The Sartorius weighing balance extends the accuracy to five decimal places.

Figure 12: Sartorius high precision weighing balance

3.3.2. Experimental Procedures

The decomposition rate of the sample was determined by placing a small amount in an alumina crucible and measuring how its weight changes with time. The initial weight of the sample was determined by measuring and subtracting the weight of sample and crucible to

the weight of the empty crucible. The crucible with the sample was left in high precision balance for one hour while recording the change in weight in every 5 minutes.

3.4. Differential Thermal Analysis

Differential thermal analysis is a type of calorimetry method that measures the temperature difference between the sample and a reference material as a function of time or temperature in a specified atmosphere. State variables of a body are measured to determine the heat transfer associated with changes of its state. Changes of the body's state can result from chemical reactions, physical changes, or phase transitions under specified constraints. An addition to DTA is differential scanning calorimetry (DSC). DSC measures the difference in the amount of heat required to increase the temperature of the sample and reference as a function of temperature. With DSC, additional information such the heat of fusion or crystallization can be measured in the sample. Other scanning devices used to investigate the thermal properties of materials include thermogravimeters (TGA) and thermal mechanical analysers (TMA).

3.4.1. Instrumentation

3.4.1.1. Differential Thermal Analyser

A Setaram 92 with TGA 92 (KEP Technologies) was used to conduct differential thermal analysis. The thermo-analyser is comprised a B92 microbalance, furnace, controller, DTA plate thermocouple, inert carrier gas, and a vacuum pump to create vacuum in the analyser before inert gas flushing. The thermal analyser was equipped with a user interface that allows the user to programme the heating and cooling operations, and periods of constant temperature for measurements.

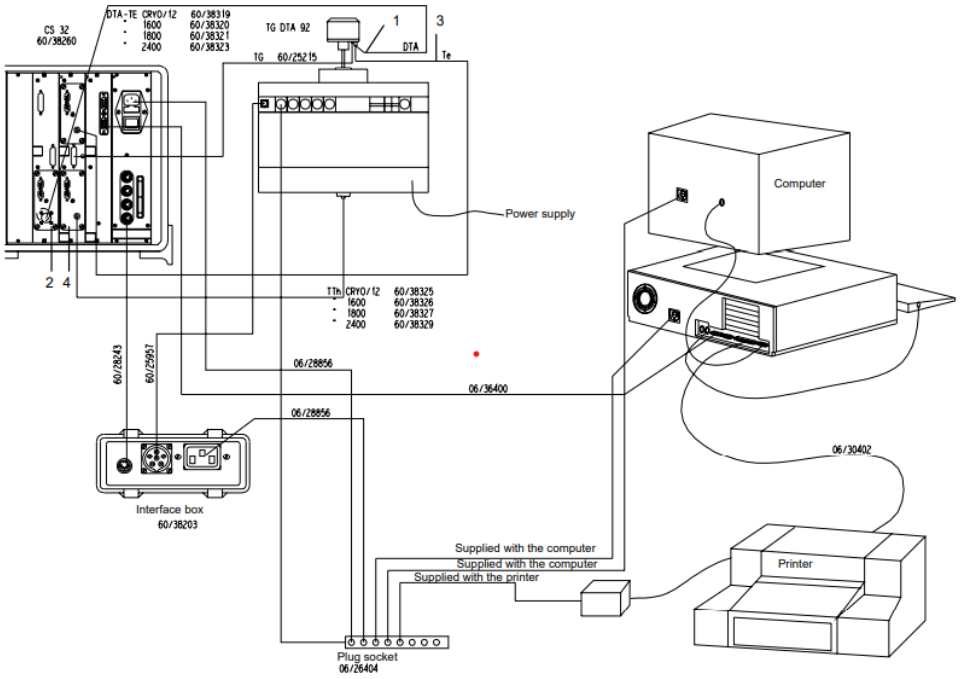

Figure 13: Setaram 92-16.18 with TGA 92 schematic (KEP Technology user manual)

Figure 13: Setaram 92-16.18 with TGA 92

3.4.2. Experimental Procedures

Analysed samples were placed in an alumina crucible for differential thermal analysis under Ar filled atmosphere glove box. The samples were transferred to the DTA in Ar containing closed boxes, and they were opened to air for approximately 1 minute for weighting and installing into the differential thermal analyser. A high precision balance (described in Section 3.3.1.1) was used to measure the weight of the samples before and after thermal analysis. In the DTA, the samples were first vacuumed and when then purged with high purity argon for 30 minutes before thermal analysis. The heating rate of the analyser was set at 5^{o}C per minute and the temperature was increased from approximately 20^{o}C to 400^{o}C. When the maximum temperature was reached, it was kept constant for a short time interval and the samples was cooled to room temperature with the same rate before repeating the heating and cooling process again.

3.5. Coin Cells

Coin cells, also known as button cells, are small single cell batteries shaped as squat cylinders. They typical sizes range from 5 to 22 mm in diameter and 6 mm in height. As mentioned in previous chapters, electrochemical cells generate electrical energy as a result of chemical reaction happening inside. Like all cells, the assembled coin cell in this research consists of a negative electrode (the anode), a positive electrode (the cathode), an electrolyte contained in between the electrodes, and a container or housing. The components of the cells are listed below:

1. Stainless steel cap and gasket
2. Stainless steel spring
3. Stainless steel spacer
4. Negative electrode (copper foil coated with active material)

5. Electrolyte (prepared samples)
6. Positive electrode (aluminium foil paper coated with active material)
7. Aluminium coated can

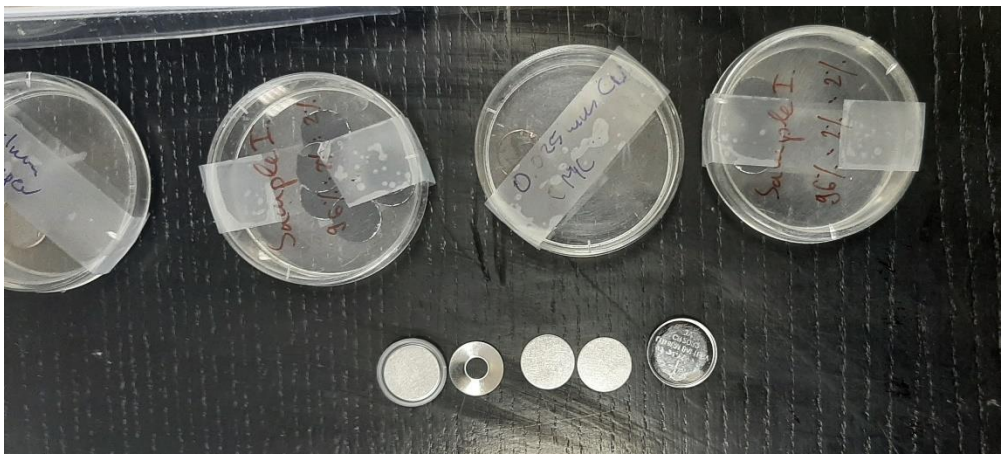

Figure 14: Coin cell components

3.4.1. Instrumentation

3.4.1.1. High precision weighing balance

A X Precision weighing balance was used to measure the stoichiometric weight of raw materials to create the active layer coat of the electrodes, and to measure the weight of electrolyte sample used in the cell. The same high precision balance was used during sample preparation and the instrument specification have been briefly explained above.

3.4.1.2. Oven

The same Memmert oven was used to dry the active medium coated on the copper (anode) and aluminium (cathode) foil paper. The oven was also used to further remove any moisture that may have been absorbed while they were being prepared for the coin cell. The specifications of the oven have already been explained above.

3.4.1.3. Hydraulic Press

A Specac manual hydraulic press was used to compress the electrolytes into pellets before being placed inside the coin cell. It was also used to press and attach the coin cell once all its components were arranged in the correct order. Specac manual hydraulic presses are designed for a wide range of laboratory press applications and can be configured to exert an adjustable load up to 250 kN.

Figure 15: Specac manual hydraulic press

3.4.1.4. Hammer and Puncher

A carbon steel hammer and stainless-steel puncher were used to punch out the desired size of electrodes coated with active materials. The desired diameter of the electrodes was 8mm.

Figure 16: Carbon steel and stainless-steel puncher.

3.4.2. Experimental Procedures

3.4.2.1. Preparation of Electrodes

Aluminium foil of 0.025mm thickness and coated with an active layer was used as the cathode of the coin cell. The active layer was composed of a mixture of $LiCoO_2$, polyvinylidene fluoride and N-methyl-2-pyrodidone. The anode of the coin cell was made of 0.025mm thick copper, also coated with an active layer. This active layer was a mixture of graphite, carbon black and carboxymethylcellulose. The table below illustrates the amount of the different reactants used to make the active materials:

Cathode	Anode
96wt% of $LiCoO_2 \approx 4.8g$	96wt% of graphite ≈2.4g
2wt% of carbon black ≈ 1.0g	2wt% of carbon black ≈ 0.05g
2wt% of polyvinylidene fluoride ≈ 0.1g	2wt% of carboxymethylcellulose ≈ 0.05g
5ml of N-methyl-2-pyrodidone	5ml of N-methyl-2-pyrodidone

Table 2: amount of reactants used to make active coat

The mixture of the reactants was then evenly spread across the surface of the aluminium and copper foil paper. The paper was then placed inside the oven for 6 hours, maintaining the temperature at 64°C, to dry. The coated electrodes were then left to cool down before being punched into circles of 8mm using a hammer and puncher.

3.4.2.2. Preparation of Electrolytes

500mg of solid electrolyte was compressed into pellets using a hydraulic press. The pellets were then placed inside the oven for heating to remove any moisture that may have been absorbed during preparation. The pellets were kept in the oven one hour while maintaining the temperature inside the oven at 90°C.

3.4.2.3. Coin Cell Assembly

The components of the coin cell were assembled using the Specac manual hydraulic press by exerting loads between 20 and 30 kN were until it was intact. The components of the cell were arranged in the following order:

1. Stainless steel cap and gasket
2. Stainless steel spring
3. Stainless steel spacer
4. Negative electrode (copper foil coated with active material)

5. Electrolyte (prepared samples)
6. Positive electrode (aluminium foil paper coated with active material)
7. Aluminium coated can

Chapter 4: Results and Discussion

4.1. Sample Preparation

Keeping track of how much reactants consumed, and products formed is important in every chemical reaction. As mentioned in the previous chapter, samples were prepared based on a study conducted by Braga et al. Approximately 10g of sample (product) was produced in each Teflon crucible after 3 hours of constant heating. The table below illustrates the weight of raw materials (reactants) used to prepare each sample:

Raw materials (reactants)	Samples produced (products)
5.860g of LiCl	≈ 10g of Li_3OCl
11.580g of LiOH	
5.899g of LiCl	≈ 10g of Li_3OCL-Ca
11.594g of LiOH	
0.071g of $Ca(OH)_2$	
5.872g of LiCl	≈ 10g of Li_3OCl-Ba
11.569g of LiOH	
0.145g of $Ba(OH)_2$	

Table 3: weight of reactants used, and products formed

After the stoichiometric amounts of raw materials were weighed, they were mixed and homogenized inside Teflon crucibles. This was done to ensure uniform distribution of raw materials in the crucibles for quick product formation. The homogenized raw materials had a thick gel like appearance with a milky white colour, as illustrated in the figure below:

Figure 17: mixed and homogenized samples before heating

The crucibles were then sealed and placed inside the oven which was used as a furnace to melt the mixed batches. The temperature of the oven was gradually increased from room temperature to 250^{o}C to avoid a temperature shock to the batches. After three hours of constant heating at 250^{o}C and subsequent cooling, white solidified bulk samples were obtained. The samples were then grinded by ball-milling using agate balls to particle sizes below 50µm before being placed in sealed containers. The containers were immediately transferred and stored to an Argon filled glove box because of their hygroscopic nature. For the same reason, only a picture of the mixed and homogenized raw materials could be captured and shown in this research; taking a clear picture of the samples would involve exposing them to moisture.

4.3. Decomposition Rate

To examine the extent of hygroscopicity of the samples, they were exposed to moisture while observing the ratio at which their weight changes. Their weight was measured and recorded over a period of one hour. The obtained results were used to calculate R.

$$R = \frac{weight\ at\ time\ t}{weight\ at\ time\ t0} \qquad (3)$$

The obtained results were then plotted for comparison and can be seen in figure below:

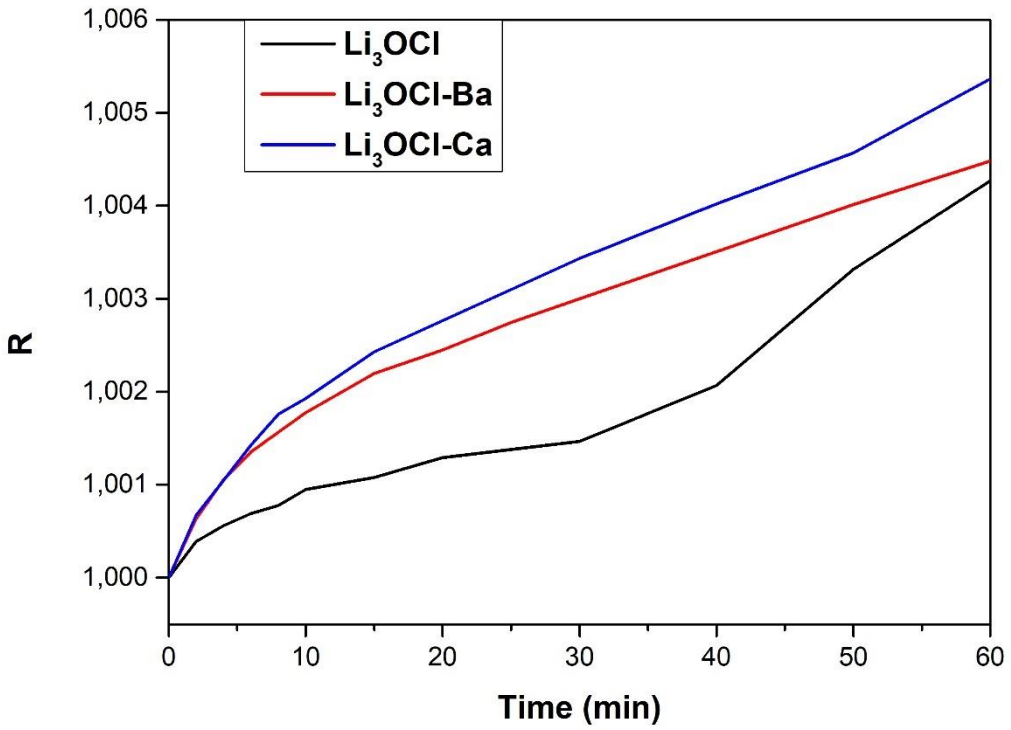

Figure 18: Relative weight change of the samples as a function of time exposed to moisture

From the obtained results, a general increase in the relative weight change all the samples was observed. This is credited to the intake/absorption of moisture by the samples from the atmosphere. As mentioned in previous chapters, the samples are highly hygroscopic and readily decompose to their starting materials as they absorb moisture, hence an increase

in weight. In addition, it was observed that the samples initially absorb water at a faster rate and this rate gradually stabilizes with time. This can also be seen from the steepness of the slope of the graphs above. The graphs initially have a steep slope, and the slope becomes smooth with time. Comparing the graphs individually, it was observed that the doped samples absorbed moisture much faster with Li_3OCl-Ca being the fastest. One can deduce that the pure Li_3OCl anti-perovskite sample is more stable and doping the sample increases the rate of hygroscopicity.

Lastly, all analysed samples were not returned into the Argon filled glove box after analysis to observe their integrity when exposed to moisture over longer periods. After few days, it was observed that the sample had become a milky gel, similar in appearance to the gel observed before the sample were prepared from the mixed and homogenized raw materials. These observations emphasized the hygroscopic nature of the sample and how proper storage, and usage is essential to maintain their integrity. On other hand, these observations also showed their environmental friendliness, as asserted in this research. The samples readily decompose to their starting materials when exposed to moisture. Unlike currently used nonaqueous electrolytes in lithium-ion batteries, these starting materials are not volatile and not corrosive. This makes discarding them much safer to the environment, and therefore a probable solution to the environmental problems posed by current electrolytes.

4.2. X-ray Diffraction

X-ray diffraction was used to analyse the microstructure of the prepared samples. As mentioned in the previous chapter, the measurements were performed in a diffractogram with a scintillation detector radiating Cu kα (γ = 1.5406 A) particles. Measurements were conducted between 15 and 100° 2Θ angles. The obtained spectra were analysed using the OriginPro program and different phases were identified using data from literature and the ICDD database. The formation of the Li_3OCl anti-perovskite phase was of great interest to verify the integrity of the prepared samples. Figure (number) below illustrates the spectra of the undoped Li_3OCl sample. Different Li_3OCl anti-perovskite planes were indexed, and the lattice parameters were determined. The cubic Li_3OCl anti-perovskite phase was identified at the peak 2Θ = 32.7° belonging to the (0 1 1) plane with Pm3m space group and a lattice constant of 3.91A.

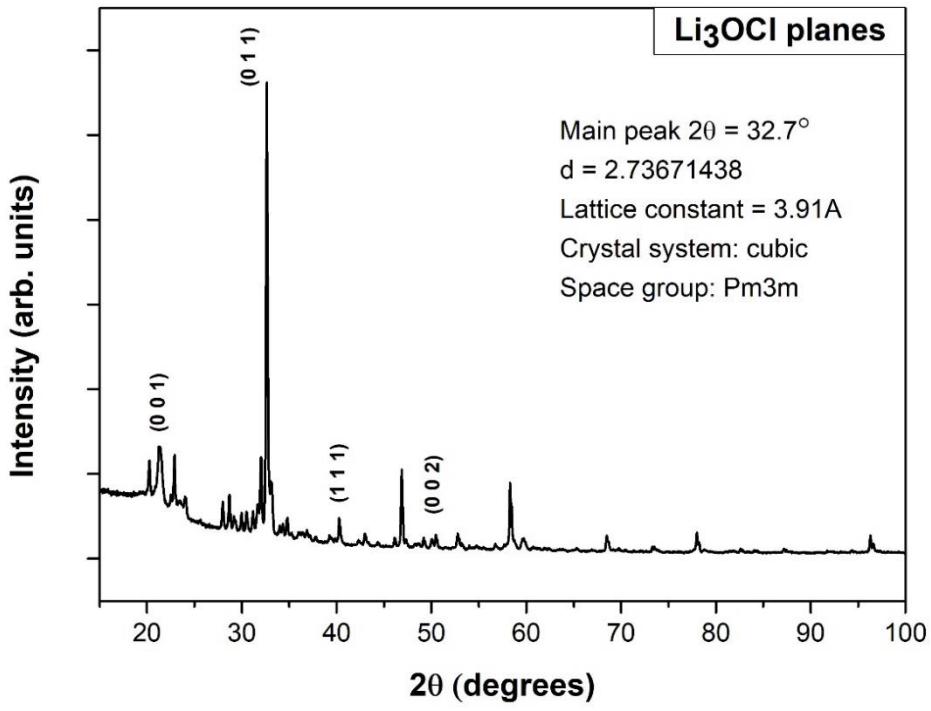

Figure 19: Li_3OCl planes of the undoped Li_3OCl sample

No significant shift in peak position of the Li_3OCl phase was observed in all the samples. However, certain planes were could not be identified in the spectra obtained from the doped samples. The figure below illustrates

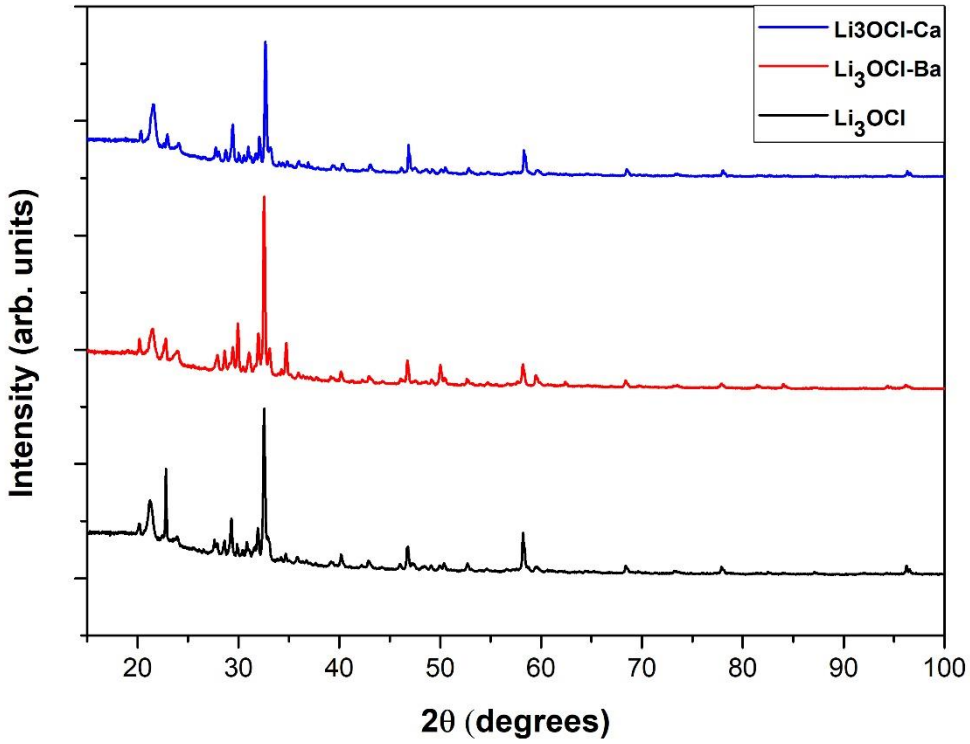

Figure 20: X-ray diffraction spectra of all prepared samples

As mentioned above, the different phases in the sample were identified using data from literature and the ICDD database and have been labelled in the figures below. For neatness, the identified phases were labelled with symbols and table (number) can be used as a reference for each symbol.

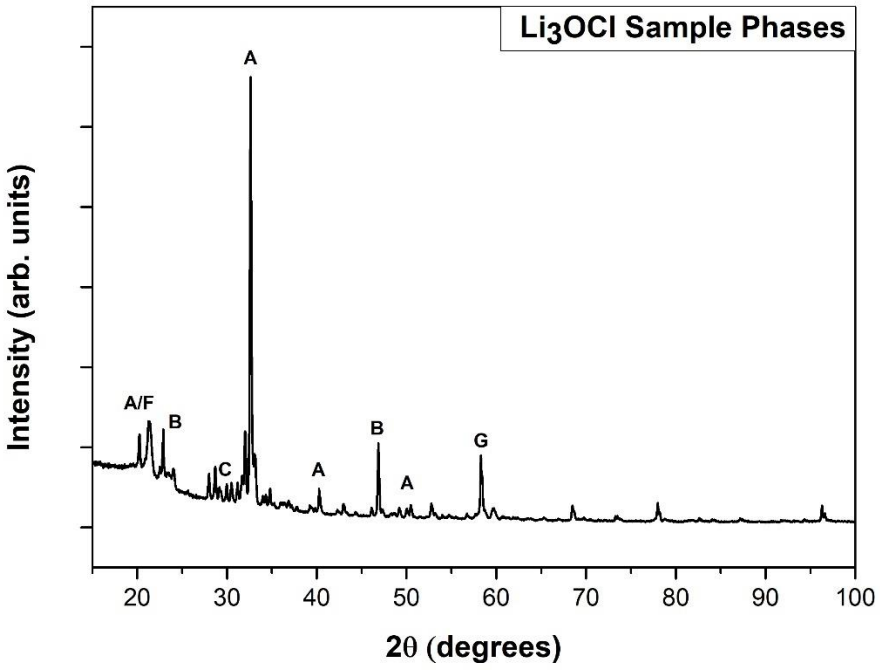

Figure 21: identified phases in the Li_3OCl sample

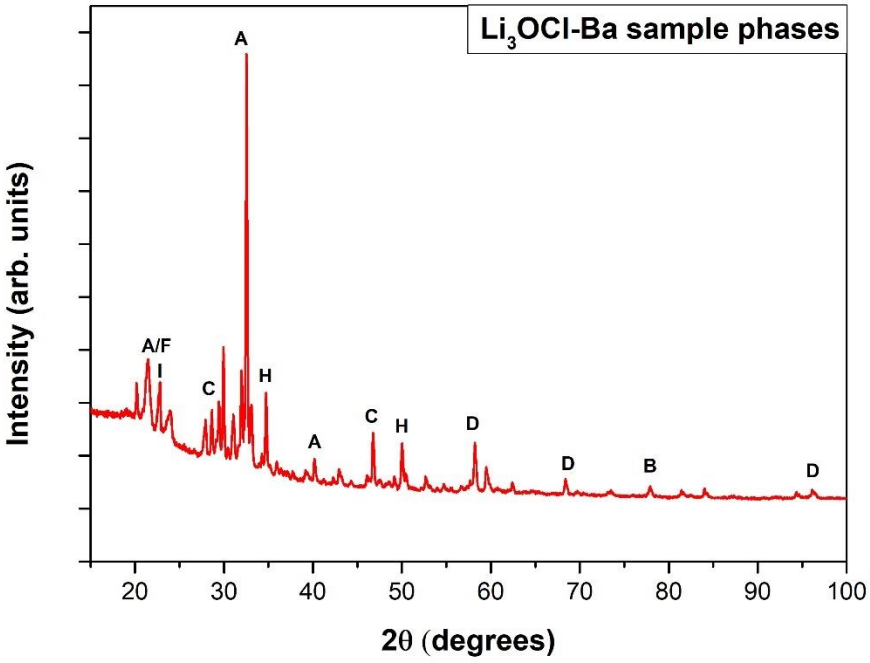

Figure 22: identified phases in the Li_3OCl-Ba sample

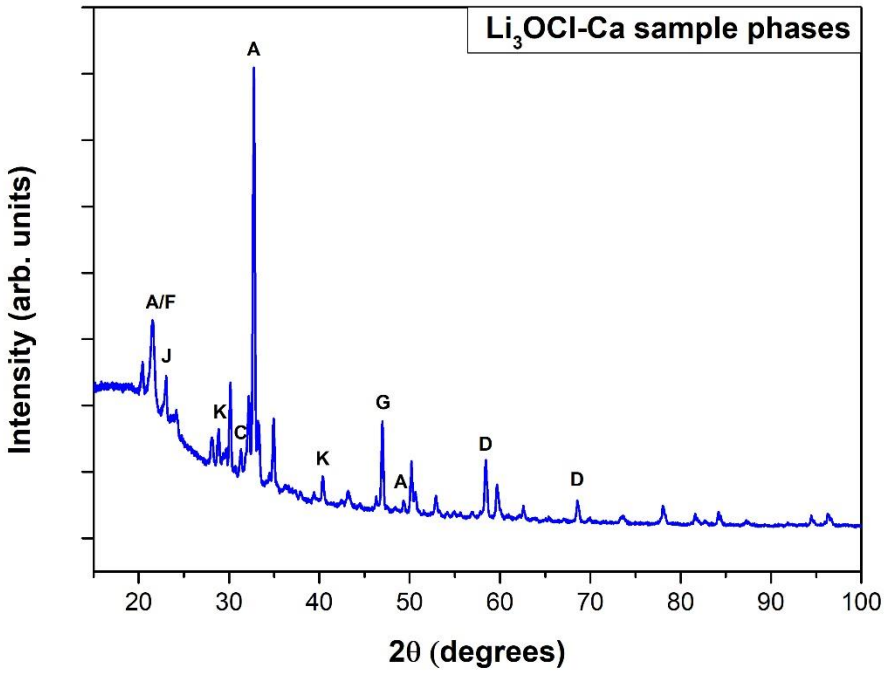

Figure 23: identified phases in the Li_3OCl-Ca sample

Symbol	Phase	2theta (Degrees)	d spacing (Armstrong)	h	k	l
A	Li_3OCl	32,700	2,736	0	1	1
		21,182	4,191	0	0	1
		40,169	2,243	1	1	1
		49,881	1,827	0	0	2
B	$LiCl (H_2O)$	22,962	3,870	0	0	2
		46,890	1,935	0	0	4
		77,999	1,224	2	0	6
C	$Li_4Cl (OH)_3$	29,300	3,046	1	2	0
		31,320	2,854	0	1	2
		46,280	1,960	2	0	2
D	Li_2O_2	58,510	1,576	2	2	0
		68,710	1,365	4	0	0
		78,290	1,220	2	2	4
		96,570	1,032	4	2	0
F	Li_2CO_3	21,340	4,160			
		31,940	2,800			
G	$Li_2Cl (OH)$	46,870	1,937			
		58,110	1,586			
H	Ba	31,530	2,835	1	0	1
		34,780	2,577	1	1	0
		50,320	1,812	2	0	0
I	$Ba (OH)_2*H_2O$	22,820	3,894	0	0	1
J	Ca	29,990	2,978	1	1	0
		42,920	2,105	2	0	0
K	CaOH	28,910	3,086			
		40,420	2,230			

Table 4: Reference for X-ray diffraction indexed phases

As mentioned in previous chapters, the samples are highly hygroscopic and readily decompose when exposed to moisture. A comparison of the intensity of the Li_3OCl $2\Theta = 32.7^o$ peak was made between samples examined with a protective cover (plastic foil of 10μm

thickness) and samples exposed to moisture. The exposed samples were first left exposed for one before diffraction measurements were conducted. Even though the 32.7^{o} peak was still observed in all samples, there was a decrease in intensity of the peak in all the exposed samples, as seen the figures below. This observation emphasized the hygroscopic nature the samples and the extent of hygroscopicity was examined the subsequent sections of this research.

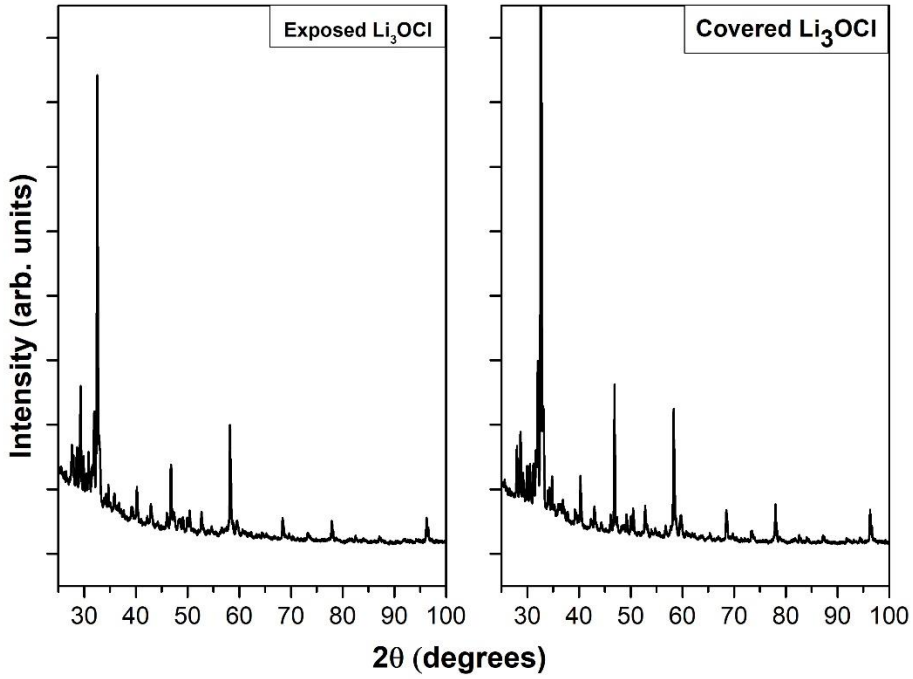

Figure 24: spectra of exposed and covered Li_3OCl samples

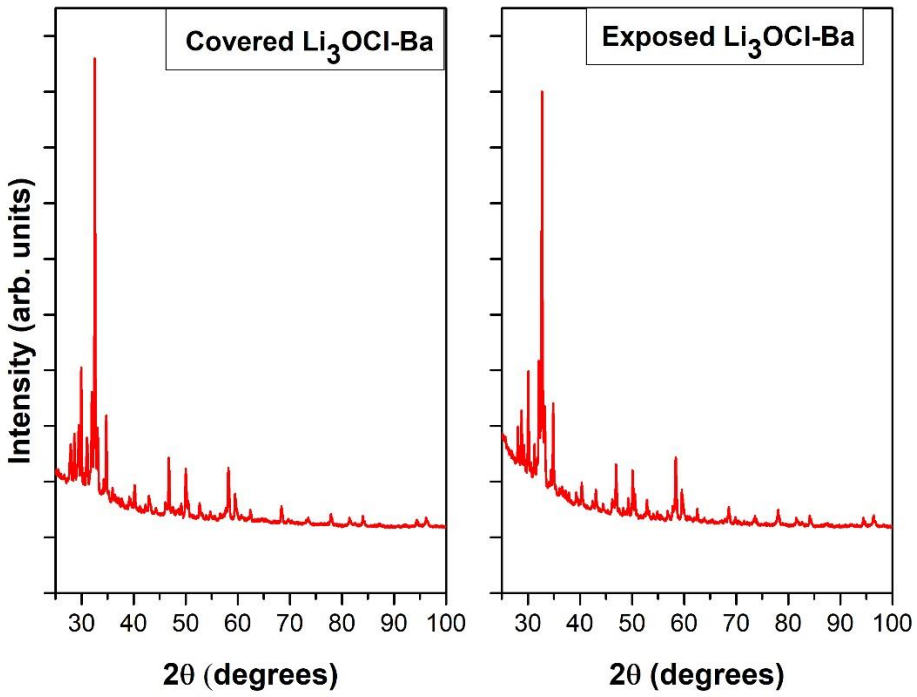

Figure 25: spectra of exposed and covered Li_3OCl-Ba samples

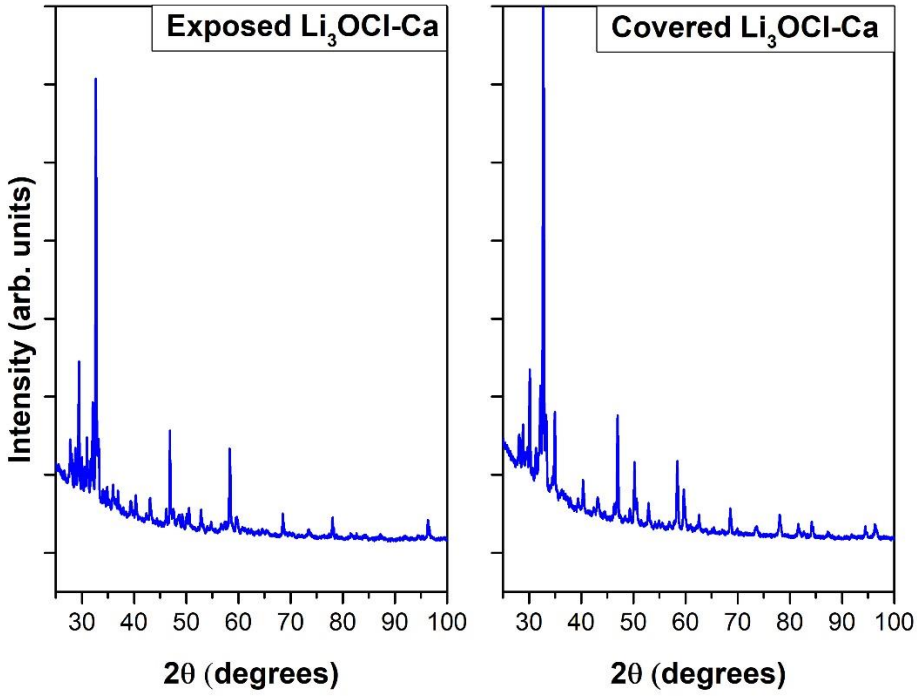

Figure 26: spectra of exposed and covered Li_3OCl-Ca sample

4.4. Differential thermal analysis

Differential thermal analysis was conducted on the samples to examine how their phases change with temperature. A series of heating and cooling steps were performed to the samples over time, while observing how heat flows in and out of the samples, and how their weight changes. The samples were heated from room temperature to approximately 400°C. This maximum temperature was held constant for a short period before cooling the sample back to room temperature. The heating and cooling process was conducted twice. Figure 27 below illustrates how the heating and cooling processes were conducted over time for all the samples. Slight deviation from the nominal constant temperature rate can be observed at the last minutes of the cooling curves due to the limited heat transfer at these temperatures in the DTA.

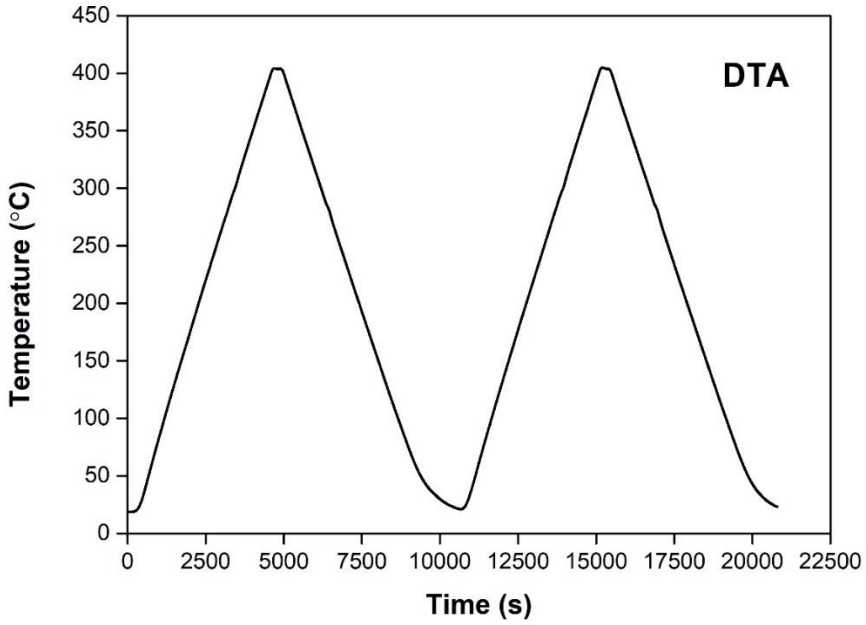

Figure 27: Heating and cooling cycles of DTA over time

The figures below illustrate the labelled endotherms of the different chemical reactions and phase transitions that took place inside the Li_3OCl sample during different

heating and cooling cycles of the thermal analysis. Positive change in heat flow from the baseline indication exothermic process.

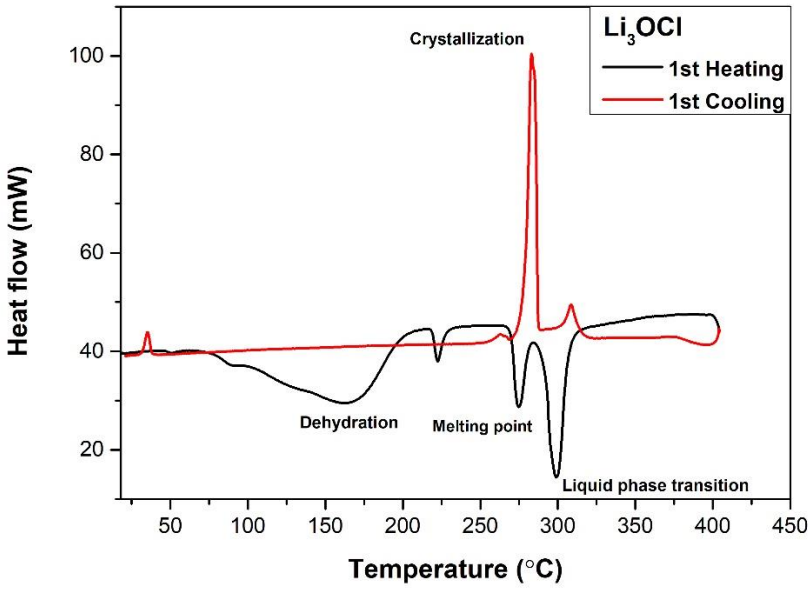

Figure 28: Heat flow in Li_3OCl during 1st heating and cooling cycles of the DTA

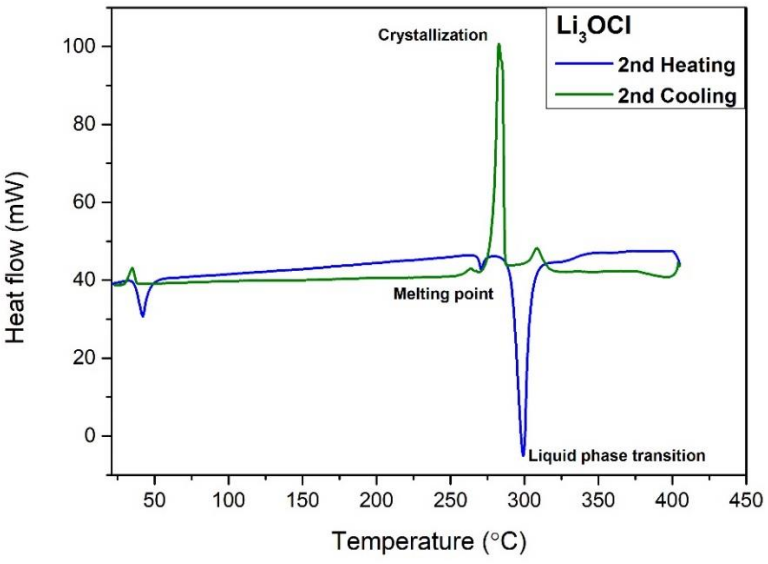

Figure 29: Heat flow in Li_3OCl during 2nd heating and cooling cycle of the DTA

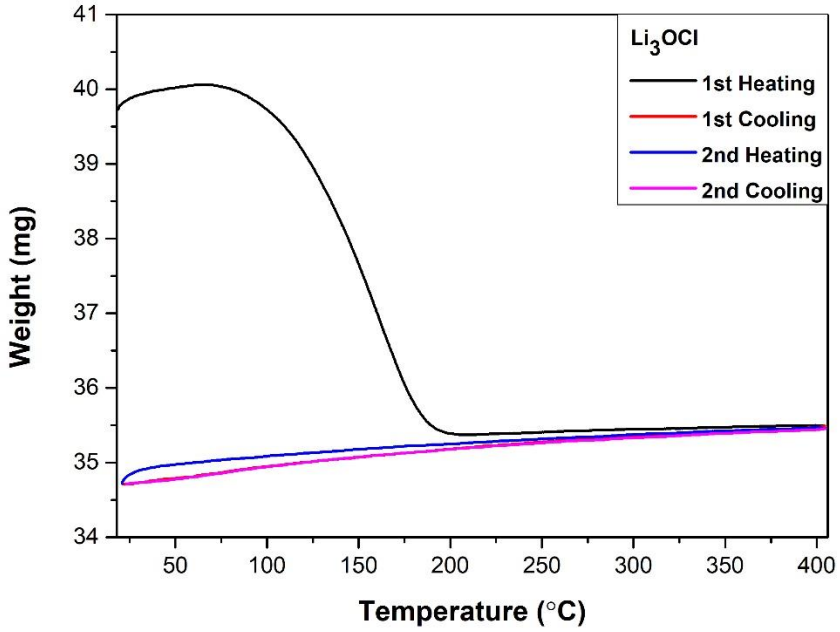

Figure 30: Weight of Li_3OCl during heating and cooling cycles

As seen in figure 27, some amount of moisture was present in the Li_3OCl sample. This is evident in the first endotherm that represents a dehydration reaction (removal of water); dehydration occurred between 83.22 and 165. 43^{o}C.This assertion can further be verified by examining how the weight the of sample changed during the 1st heating process of the experiment, shown in figure 30. The weight of the sample decreased by approximately 4.5mg and remained constant for subsequent cooling, heating, and cooling cycles. It is possible that water may have absorbed by the sample during the process removing it from the Argon filled glove box, measuring its weight, and placing it inside the differential thermal analysers. Subsequent endotherms of the experiment represent the melting point, liquid phase transition and crystallization of the 1st cooling, and 2nd heating and cooling processes; the weight of the samples remained constant after dehydration of absorbed moisture.

The same analysis was extended to the doped Li_3OCl-Ba and Li_3OCl-Ca samples. Observations consistent to those seen in the undoped Li_3OCl samples were observed:

- Dehydration and weight loss of the samples occurred during the 1st heating cycle (seen on the 1st endotherm).
- Subsequent endotherms showed the melting point, liquid transition and crystallization phase transitions of the 1st cooling, and 2nd heating and cooling cycles of the experiment.

In addition, the relative weight change and relative heat flow of all the samples was calculated and expressed in graphical figures for better comparison of data. The calculations were performed using the equations below:

$$\text{Relative heat flow} = \frac{heat\ flow\ at\ time\ t - heat\ flow\ at\ time\ t0}{mi} \qquad (4)$$

$$\text{Relative weight change} = \frac{weight\ at\ time\ t - weight\ at\ time\ t0}{mi} \qquad (4)$$

Where Mi is the initial mass of the samples before they were placed in the differential analyser:

Mi Li_3OCl = 47.66mg

Mi Li_3OCl-Ca = 72.11mg

Mi Li_3OCl-Ba = 35.33mg

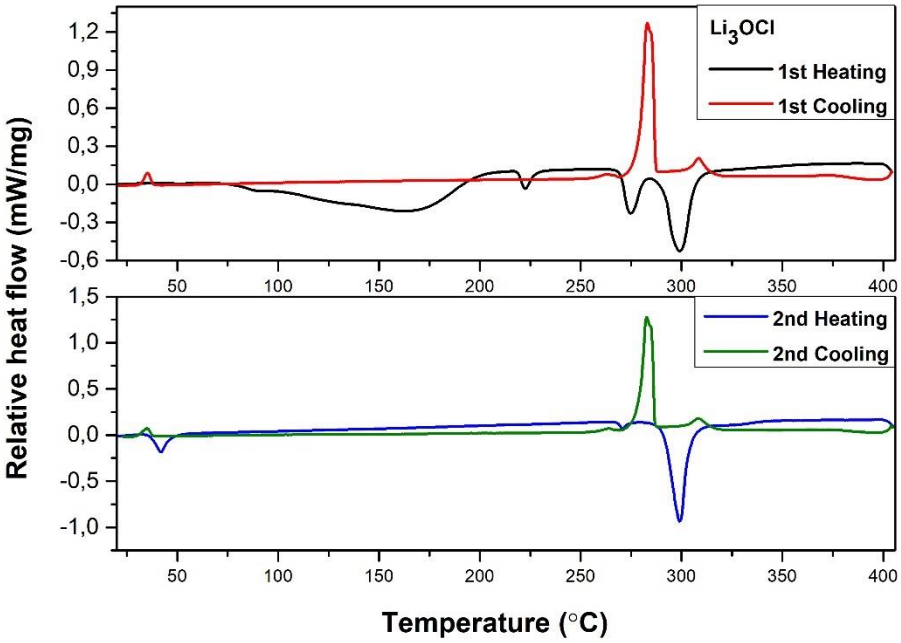

Figure 31: relative heat flow in Li_3OCl during heating and cooling cycles

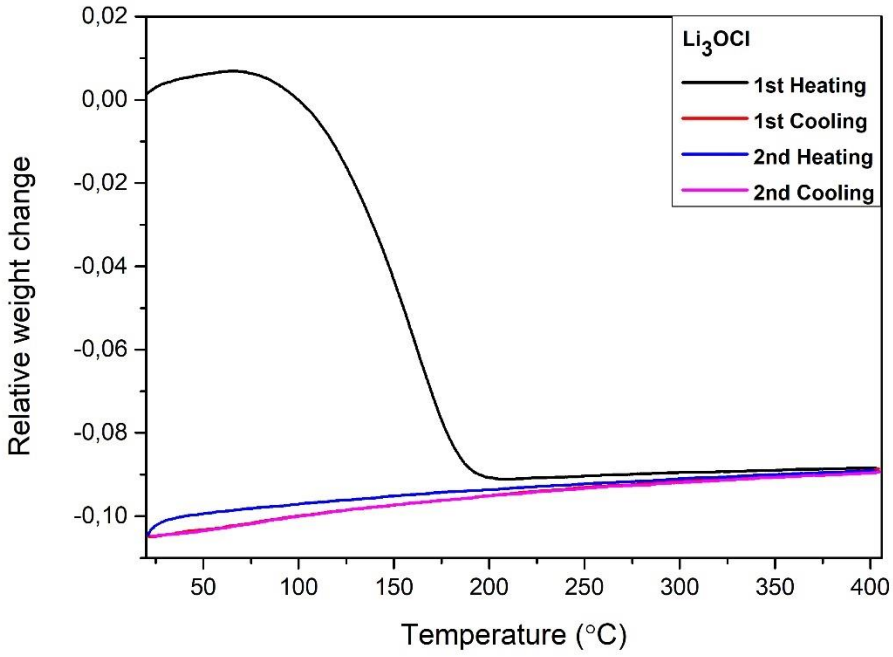

Figure 32: relative weight change of Li_3OCl during heating and cooling cycles

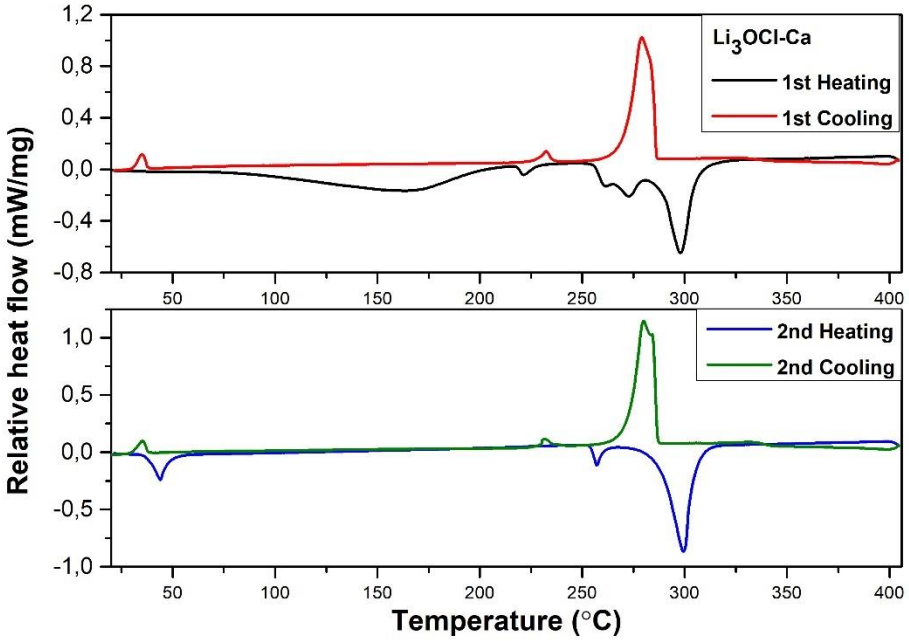

Figure 33: relative heat flow in Li_3OCl-Ca during heating and cooling cycles

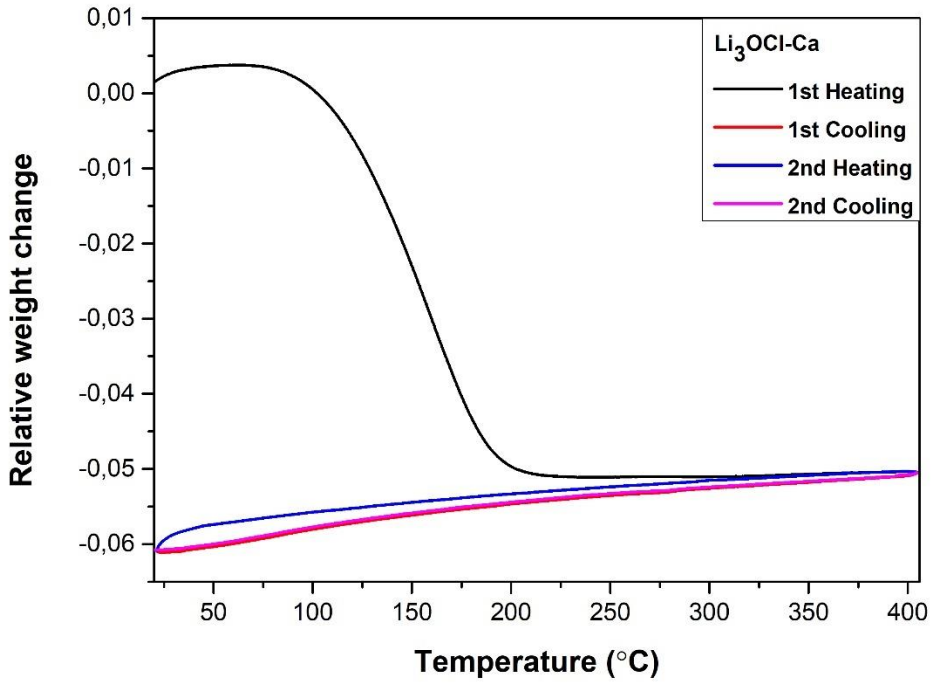

Figure 34: relative weight change of Li_3OCl-Ca during heating and cooling cycles

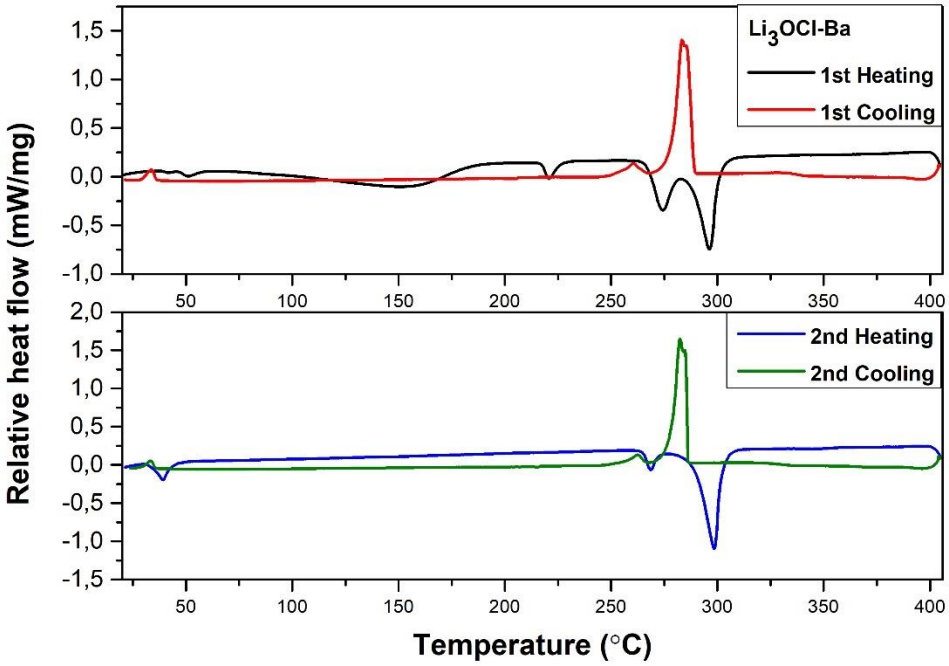

Figure 35: relative heat flow in Li_3OCl-Ca during heating and cooling cycles

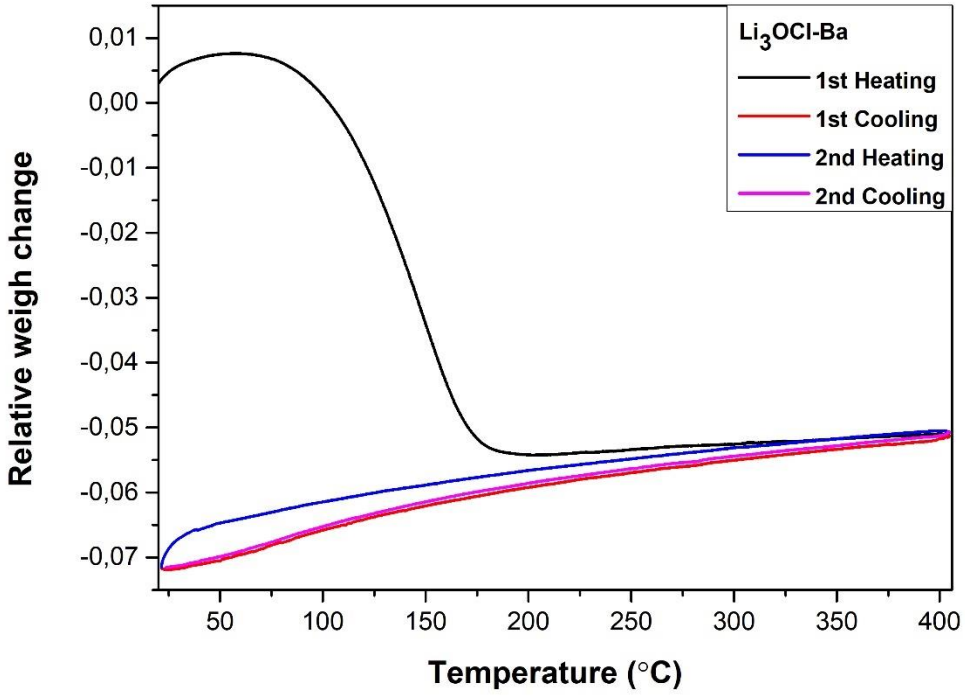

Figure 36: relative weight change of Li_3OCl-Ba during heating and cooling cycle

Furthermore, the data obtained from DTA was used to determine calorimetric data of the different heating cycles in all samples. A baseline was fit on key peaks and the area under these peaks was calculated. By doing this, the temperatures of the labelled phase transitions (dehydration, melting point, and liquid phase) were obtained and illustrated in the tables below:

Sample	**Dehydration peak**		**Melting point peak**		**Liquid phase transition peak**	
	Temperature	**Energy**	**Temperature**	**Energy**	**Temperature**	**Energy**
Li_3OCl	82.22 – 165.43°C	-124.77J/g	256.93°C	-57.271J/g	284.69°C	-125.37J/g
Li_3OCl-Ca	65.01 – 164.41°C	-234.25J/g	268.62°C	-41.8J/g	289.58°C	-125.23J/g
Li_3OCl-Ba	71.26 – 141.34°C	-153.77 J/g	265.61°C	-66.845J/g	284.54°C	-117.3J/g

Table 5: calorimetric data of the 1st heating cycle of all samples

Sample	**Melting point peak**		**Liquid phase transition peak**	
	Temperature	**Energy**	**Temperature**	**Energy**
Li_3OCl	266.95°C	-5.5399J/g	290.57°C	-159.03J/g
Li_3OCl-Ca	253.75°C	-10.96J/g	284.23°C	-159.06J/g
Li_3OCl-Ba	264.75°C	17.381J/g	286.68°C	-165.82J/g

Table 6: calorimetric data of 2nd heating cycle of all samples

4.5. Cell preparation

4.5.1. Preparation of electrodes

Electrodes are one of the key components of any cell or battery. They enable the transportation of electrons between the external circuit of the cell, and the electrolyte within the local half-cell. Therefore, precision is equally important when preparing the electrodes. Ensuring that the exact amount of raw materials was used to make the active layer coat was the most important step of preparing the electrodes. It was observed that incorrect measurements affected the viscosity of the active layer coat and cracks were observed on the layer after heating. In addition, evenly spreading a thick active layer across the aluminium and copper foil papers ensured the layer was smooth and stayed intact on the foil after heating. A comparison between a well prepared and bad active layer coat on foil paper can be seen in the figure below:

Figure 37: a smooth and thick active layer coat on foil paper (left) vs uneven and cracked active layer coat on foil paper (right)

The bad active layer coat (on the right) lost its integrity and began to crack after heating. This was because of not evenly spreading a thick layer across the foil. As seen in the picture, the layer is smooth on top and begins to crack as you move downwards. After this observation, extra caution was taken when measuring and mixing the raw material, and when evenly spreading a thick layer across the foil. This resulted into an electrode with a smooth and stable layer after heating, as seen on the left of figure 37.

As mentioned in experimental procedures followed during preparation, the coated electrodes were punched into circles of 8mm diameter using a hammer and puncher. Caution was also taken during this final step of electrode preparation. This was done to ensure that all the electrodes are punched into equal sizes for the coin cell assemble and to also not scratch or peel off the active layer coat on the foil paper. The punched electrodes can be seen on the figure below:

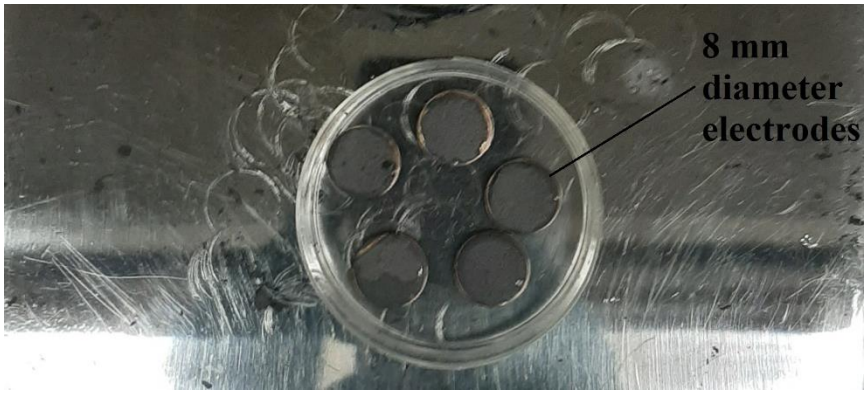

Figure 38: 8mm diameter punched electrodes with active layer coat

3.5.2. Prepared of electrolytes

As mentioned in previous chapters, a good electrolyte allows the free transport of ions/electrons. For the coin cell assembly, the prepared electrolyte samples had to be compressed into pellets using a hydraulic press. Initially, different amounts of electrolytes were weighed and compressed into pellets to assemble the coin cells. It was observed that to

obtain the right thickness for the pellets that efficiently separate the electrodes, and small enough to fit in the cell, approximately 500mg of solid electrolyte had to be used. This resulted into a good pellet for the cell that also maintained its integrity during heating when it was placed inside the oven for one hour to remove any accumulated water, as illustrated in the figure below:

Figure 39: electrolytes compressed into pellets for coin cell assembly

3.5.3. Coin cell assembly

Once the electrodes and electrolytes were prepared, the coin cells were assembled. As mentioned in the experimental procedures, the components of the cell were assembled in the order listed below:

8. Stainless steel cap and gasket
9. Stainless steel spring
10. Stainless steel spacer
11. Negative electrode (copper foil coated with active material)
12. Electrolyte (prepared samples)
13. Positive electrode (aluminium foil paper coated with active material)

14. Aluminium coated can

After the components were arranged in the right order, the coin cells were assembled using the Specac manual hydraulic press. Only loads between 20 and 30 kN were exerted to the cell until it was intact. It was observed that, exerting smaller forces was not sufficient for the components to stay intact and the cell simply fell apart. Furthermore, exerting higher loads crushed the compressed electrolyte pellets.

Assembling the coin cells involved a lot of trial and error. Finding the right amount of solid electrolyte to compress into pellets and determining exact amount of force to use to assemble the components of the cell was essential to this research. After different attempts, well intact coin cells were obtained.

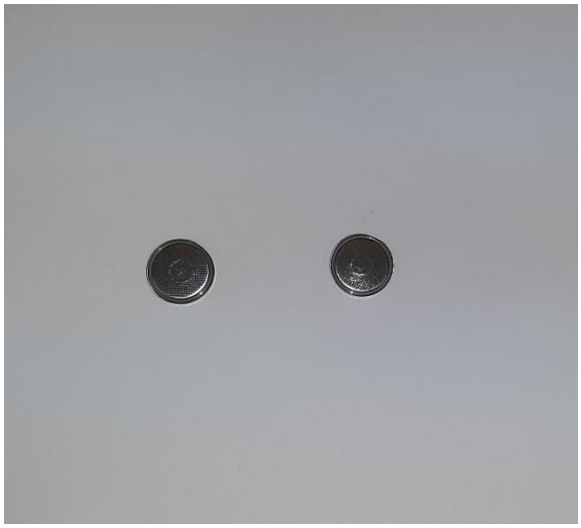

Figure 40: assembled coin cells

After preparing the samples, conducting X-ray diffraction, differential thermal analysis, determining the rate at which the samples decompose, and assembling the coin cells, the final task of this research was to examine the ionic conductivity of the proposed electrolytes. The coin cell assembled with pure Li_3OCl sample was used to connect an electrical circuit with 1.4A flowing through it. The electrical circuit was connected

immediately after the cells were assembled. An accumulation of heat was observed on the cells as it successfully enabled current to flow through them. This observation showed that the proposed electrolytes can enable electron/ion transport. Furthermore, when the current was disconnected and a voltmeter was immediately placed, a potential difference of 2V was recorded across the cells. However, the extent at which they transport electrons/ions could not be examined. When the electrical circuit was reconnected after five minutes, the coin cells did not allow current to flow and potential difference of 0V was recorded in subsequent measurements. It was also observed that the solid electrolytes had accumulated a significant amount of moisture and the assembled coin cells fell apart after a few days; the electrolytes pellets turned into a milky white gel. This explains why the coin cells only allowed current to flow after they were immediately assembled and could not after a short period of time.

These key observations re-emphasized the hygroscopic nature of the prepared electrolytes. With the available equipment, properly sealed coin cells could not be assembled, and subsequent ionic conductivity measurements could not be conducted. Even though the electrolytes do enable the transportation of ion, they are highly hygroscopic. They lose their integrity and ionic transport ability quickly when exposed to moisture. From these findings, optimum coin cells can only be assembled with the proper crimping press. With the right equipment, a well-sealed cell can be assembled that does not allow any moisture to go into the electrolyte. This would in turn ensure the electrolyte restores its integrity and ability ionic transport ability, making future conductivity measurements possible.

Chapter 5: Conclusion and Recommendation

In this research, a new class of lithium-rich anti-perovskite materials have been subjected to structural and thermal characterization for solid state batteries as substitutes for currently used organic liquid electrolytes which are toxic and flammable. Three lithium-rich anti-perovskite samples (Li_3OCl, Li_3OCl-Ba and Li_3OCl-Ca) were prepared and analysed using X-ray diffraction, thermal differential analysis, the rate at which they decompose when exposed to moisture and used to assembled coin cells. The samples were prepared based on a study conducted by Braga et al. The general equation of their composition is $A_{3-2x}M_xO_{1+y}Cl_{1-2y}$ (where A=Li; M= Ba, and Ca; x= 0.005; y=0). The resulting samples are Li_3OCl, $Li_{2.99}Ca_{0.005}OCl$, $Li_{2.99}Ba_{0.005}OCl$, and $Li_{2.99}Mg_{0.005}OCl$. For simplicity, the samples were referred to as Li_3OCl, Li_3OCl-Ba and Li_3OCl-Ca in this research. It is important to mention that the prepared are highly hygroscopic and were mostly kept in an Argon filled glove box to protect them from moisture; the samples readily decompose when exposed to moisture.

X-ray diffraction was used to identify the different crystalline/semi-amorphous phases in the sample. Differential thermal analysis was used to determine different calorimetric data and phase transitions during heating and cooling cycles. The samples were then used to assembled coin cells for ionic conductivity measurements. After immediate assembly, the cells were connected to a circuit with 1.4A current. A potential different of 2V was recorded across the cell, showing that materials do enable Li ion transport. However, the extent at which they transport electrons/ions could not be examined. When the electrical circuit was reconnected after five minutes, the coin cells did not allow current to flow and potential difference of 0V was recorded in subsequent measurements. It was also observed that the solid electrolytes had accumulated a significant amount of moisture and the assembled coin cells fell apart after a few days; the electrolytes pellets turned into a milky white gel. This

explains why the coin cells only allowed current to flow after they were immediately assembled and could not after a short period of time.

These key observations re-emphasized the hygroscopic nature of the prepared electrolytes. With the available equipment, properly sealed coin cells could not be assembled, and subsequent ionic conductivity measurements could not be conducted. Even though the electrolytes do enable the transportation of ion, they are highly hygroscopic. They lose their integrity and ionic transport ability quickly when exposed to moisture. From these findings, optimum coin cells can only be assembled with the proper crimping press. With the right equipment, a well-sealed cell can be assembled that does not allow any moisture to go into the electrolyte. This would in turn ensure the electrolyte restores its integrity and ability ionic transport ability, making future conductivity measurements possible. In conclusion of the research, the extent of hygroscopicity of the samples was examined by exposing them to moisture and observing their relative weight change as they absorb moisture.

Chapter 6: Reference

Cairns, E. (2004). Batteries, Overview. *Encylopediua of Energy, 1*, 117-126.

Chen, K., Li, C., Hu, M., Chen, Z., & Li, C. (2017). Deformation Modes and Anisotropy of Anti-Perovskite Ti3AN (A = Al, In and Ti) from First-Principle Calculations. *Materials, 10*.

Fabian , M., Tolnai, I., Khanna, A., Horvath, Z. A., Kovacs Kis, V., & Kovacs, Z. (2021, January 12). Structural Characterization of Oxyhalide Materials for Solid-State Batteries. *Physica Status Solidi*.

John Wiley & Sons, Inc. (2011, September 17). *Electrochemical Cells: The Daniell Cell*. Retrieved from Dummies: https://www.dummies.com/education/science/chemistry/electrochemical-cells-the-daniell-cell/

Li, M., Lu, J., Chen, Z., & Amine, K. (2018). 30 Years if Lithium-Ion Batteries. *Advanced Materials*. doi: 10.1002/adma.201800561

Liu, K., Liu, Y., Pei, A., & Cui, Y. (2018). Materials for Lithium-ion Battery Safety. *Science Advances*.

Lu, X., Wu, G., Howard, J. W., Chen, A., Zhao, Y., Daemen, L. L., & Jia, Q. (2014). Li-rich Anti-perovskite Li3OCl Films with ENhanced Ionic Conductivity. *Royal Society of Chemistry* , 11520-11522.

Lu, X., Wu, G., Howard, J. W., Chen, A., Zhao, Y., Daemen, L. L., & Jia, Q. (2014). Li-Rich Anti-Perovskite Li3OCl Films with Enhanced Ionic Conductivity. *Royal Society of Chemistry*, 11520-11522.

Manthiram, A. (2017). An Outlook on Lithium Ion Battery Technology. *ACS Central Science* , 1063-1069.

Shah Bukhari, S., Maqsood, J., Baig, M. Q., Ashraf, S., & Khan, T. A. (2015). Comparison of Charasteristics- Lead Acid, Nickel Based, Lead Crystal and Lithium Based Batteries. *AKSIM-AMSS International Conference on Modelling and Simulation* (pp. 444-450). Islamabad: IEEE Computer Society.

University of Illinois. (2014, December 18). *Development of X-rays Crystallography* . Retrieved from Publish.illiniis.edu: https://publish.illinois.edu/x-raycrystallography/2014/12/18/introduction/

Wagner, R., Preschitschek, N., Passerini, S., Leker, J., & Winter, M. (2013). Current research trends and prospects among the various materials and designs used in lithium-based batteries. *Journal of Applied Chemistry, 43*, 481-496.

Yang, Y., DeVita, M., Lee, S. S., & Kim, J. C. (2020, September 29). Lithium and Chlorine-Rich Preparation of Mechanochemically Activated Anti-Perovskites Composites for Solid State Batteries. *Frontiers in Chemistr*, pp. 1-7.

Yoshino, A. (2014). Development of the Lithium-Io Battery and Recent Technological Trends. In G. Pistoia, *Lithium-Ion Batteries: Advances and Applications* (pp. 1-20). Amsterdam: Elsevier.

Zhao, Y., & Daemen , L. L. (2012). Superionic Conductivity in Lithium-Rich Anti-Perovskites. *Journal of the American Chemical Society* , 15042-15047.

Zubi, G., Dufo-Lopez, R., Carvalho, M., & Pasaoglu, G. (2018). The Lithium-ion Battery: Sate of the Art and Future Perspectives. *Renewable and Sustainable Energy Reviews*, 292-308.